AD-A266 507

[DOCU]MENTATION PAGE

Form Approved OMB No. 0704-0188

[...] estimated to average 1 hour per response including the time for reviewing instructions, searching existing data sources [...] ing and reviewing the collection of information. Send comments regarding this burden estimate or any other aspect of this [...] ing this burden to Washington Headquarters Services, Directorate for Information Operations and Reports, 1215 Jefferson [...] to the Office of Management and Budget, Paperwork Reduction Project (0704-0188), Washington DC 20503

2. REPORT DATE	3. REPORT TYPE AND DATES COVERED
6/25/93	Interim 6/1/92-5/31/93

4. TITLE AND SUBTITLE

Methods of Tunneling Spectroscopy with the STM

5. FUNDING NUMBERS

Grant N00014-91-J-1629
R&T Code 413S001

6. AUTHOR(S)

R. J. Hamers

7. PERFORMING ORGANIZATION NAME(S) AND ADDRESS(ES)

Department of Chemistry
University of Wisconsin-Madison
1101 University Avenue
Madison, WI 53706-1396

8. PERFORMING ORGANIZATION REPORT NUMBER

9. SPONSORING/MONITORING AGENCY NAME(S) AND ADDRESS(ES)

Office of Naval Research, Chemistry
800 North Quincy Street
Arlington, VA

10. SPONSORING/MONITORING AGENCY REPORT NUMBER

14

DTIC ELECTE JUL 07 1993 S B D

11. SUPPLEMENTARY NOTES

12a. DISTRIBUTION/AVAILABILITY STATEMENT

Unlimited

DISTRIBUTION STATEMENT A
Approved for public release;
Distribution Unlimited

12b. DISTRIBUTION CODE

13. ABSTRACT *(Maximum 200 words)*

The theory and application of scanning tunneling spectroscopy techniques is reviewed. Methods of acquisition and analysis are treated in detail, with examples from the scientific literature.

93 7 06 016

93-15291

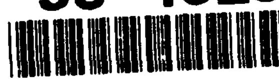

14. SUBJECT TERMS

Scanning tunneling microscopy, STM, surfaces, semiconductors, photovoltage, silicon

15. NUMBER OF PAGES

31 total

16. PRICE CODE

---

17. SECURITY CLASSIFICATION OF REPORT	18. SECURITY CLASSIFICATION OF THIS PAGE	19. SECURITY CLASSIFICATION OF ABSTRACT	20. LIMITATION OF ABSTRACT
Unclassified	Unclassified	Unclassified	UL

DISCLAIMER NOTICE

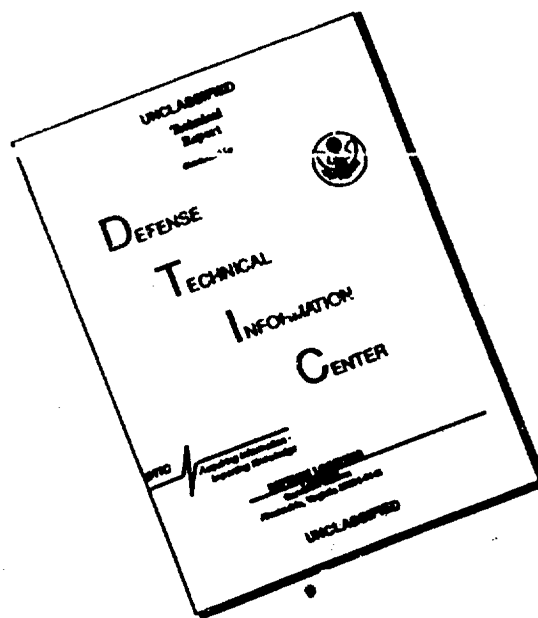

THIS DOCUMENT IS BEST QUALITY AVAILABLE. THE COPY FURNISHED TO DTIC CONTAINED A SIGNIFICANT NUMBER OF PAGES WHICH DO NOT REPRODUCE LEGIBLY.

U.S. OFFICE OF NAVAL RESEARCH

GRANT N00014-91-J-1629

R&T Code 413S001

Technical Report #14

Methods of Tunneling Spectroscopy with the STM

by

R.J. Hamers

Prepared for Publication

in

Scanning Tunneling Microscopy: Theory, Techniques, and Applications

June 25, 1993

Department of Chemistry
University of Wisconsin-Madison
Madison, WI 53706

Reproduction in whole or in part is permitted for any purpose of the United States Government.

This document has been approved for public release and sale: its distribution is unlimited.

Scanning Tunneling Microscopy and Spectroscopy

Theory, Techniques, and Applications

DTIC QUALITY INSPECTED 5

EDITOR

Dawn A. Bonnell

Accession For	
NTIS GRA&I	☑
DTIC TAB	☐
Unannounced	☐
Justification	
By	
Distribution/	
Availability Codes	
Dist	Avail and/or Special
A-1	

Dawn A. Bonnell
Department of Materials Science and Engineering
University of Pennsylvania
Philadelphia, PA 19104-6272

Library of Congress Cataloging-in-Publication Data

Scanning tunneling microscopy and spectroscopy : theory, techniques, and applications / editor, Dawn A. Bonnell.
p. cm.
Includes bibliographical references and index.
ISBN 0-89573-768-X.
1. Scanning tunneling microscopy. 2. Tunneling spectroscopy.
I. Bonnell, Dawn A.
QH212.S35S365 1993
502'.8'25—dc20 92-46997

©1993 VCH Publishers, Inc.
This work is subject to copyright.
All rights reserved, whether the whole or part of the material is concerned, specifically those of translation, reprinting, re-use of illustrations, broadcasting, reproduction by photocopying machine or similar means, and storage in data banks.
Registered names, trademarks, etc., used in this book, even when not specifically marked as such, are not to be considered unprotected by law.

Printed in the United States of America

ISBN 0-89573-768-X VCH Publishers, Inc.
ISBN 3-527-27920-2 VCH Verlagsgesellschaft

Printing History:
10 9 8 7 6 5 4 3 2 1

Published jointly by

VCH Publishers, Inc.
220 East 23rd Street
New York, New York 10010

VCH Verlagsgesellschaft mbH
P.O. Box 10 11 61
D-6940 Weinheim
Federal Republic of Germany

VCH Publishers (UK) Ltd.
8 Wellington Court
Cambridge CB1 1HZ
United Kingdom

Preface

Scanning tunneling microscopy (STM), tunneling spectroscopy (STS), and atomic force microscopy (AFM) have evolved into routine surface characterization tools. The question arises: from where can one learn the basic operating principles and techniques of scanned probe microscopies? Hundreds of research papers are published each year which either focus on a particular aspect of the measurement or use STM techniques in passing. These papers are usually directed towards the expert and, consequently, are not very helpful to the novice. Even if this were not the case, the prospective STM user would face the daunting task of sifting through nearly 1000 papers to glean the introductory concepts. Assistance might be found in several of the excellent review articles published in the last eight years, such as those by P. Hansma and J. Tersoff, Y. Kuk and J. Silverman, and H. Rohrer, but even these papers cannot address all of the relevant background required for a beginner.

As the use of STM became more common through access to commercial microscopes, several approaches to teaching STM and AFM have been taken. Scientific societies (the Materials Research Society, the American Vacuum Society, etc.) offer one- or two-day courses on the applications of STM/AFM and, of course, microscope companies supply some instruction with their instruments. Aspects of both STM and AFM are currently introduced in upper level courses offered at universities in physics, materials science, and chemical engineering departments. At present, no text exists upon which to base such courses or to develop alternative instructional formats.

Monographs do exist which serve as overviews of the field at the time of their publication. Notable examples include books edited by R. J. Bohm, N. Garcia,

CHAPTER

4

Methods of Tunneling Spectroscopy with the STM

R. J. Hamers

The University of Wisconsin
Madison, WI 53706

4.1 Introduction
4.2 One-Dimensional Tunneling
4.3 Voltage-Dependent STM Imaging
  4.3.1 Experimental Technique
  4.3.2 Interpretation of Voltage-Dependent STM Images
  4.3.3 Applications of Voltage-Dependent STM Imaging
4.4 Modulation Techniques: STM
  4.4.1 Experimental Techniques
  4.4.2 Interpretation
  4.4.3 Experimental Applications of STS
4.5 Local *I–V* Measurements
  4.5.1 Experimental Methods
  4.5.2 Analysis and Interpretation of *I–V* Data
  4.5.3 Comparison of Normalized *I–V* Data with True DOS
  4.5.4 Applications of Local *I–V* Spectroscopy
4.6 General Features of Tunneling Spectra
  4.6.1 Dynamic Range
  4.6.2 Resolution
  4.6.3 Tip Electronic Structure
  4.6.4 Anomalies
4.7 Other Spectroscopies
  4.7.1 Inelastic Tunneling Spectroscopy
  4.7.2 Barrier Height Spectroscopy
4.8 Summary

4.1 Introduction

One of the most exciting aspects of scanning tunneling microscopy is that in addition to providing information on the local "topographic" structure of the surface, the images inherently contain a large amount of data relating to the local *electronic* structure of the surface. Tunneling spectroscopy has its origins in some of the earliest STM work of Binnig et al., who found evidence for voltage-dependent changes in the appearance of some of the atoms within the (7×7) unit cell and correctly noted that such effects might arise from tunneling

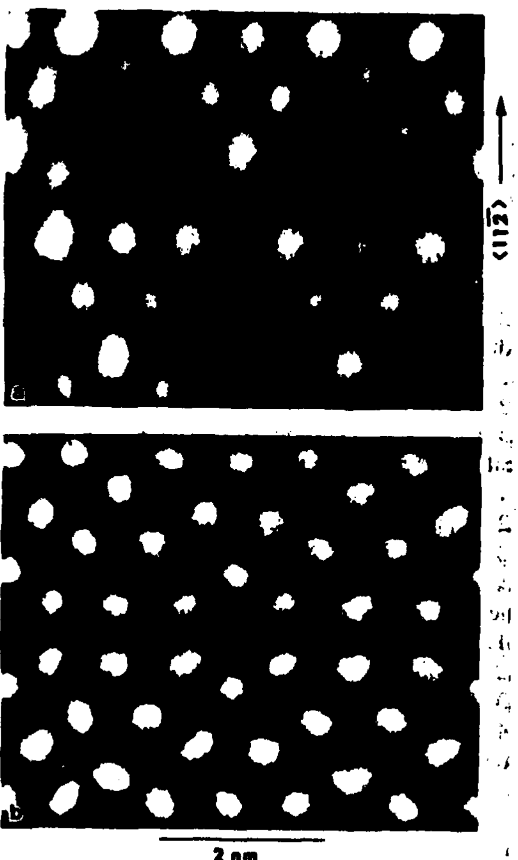

Figure 4.1 STM images of Si(111)-(7×7) acquired at positive and negative sample bias. **(a)** Sample biased at −2 V, showing stacking fault-related asymmetries. **(b)** Sample biased at +2 V, revealing symmetric-appearing unit cell. (Reprinted with permission from Ref. [3].)

through discrete electronic states of the sample.[1] These voltage-dependent changes in appearance are clearly seen in Figure 4.1, which shows STM images of Si(111)-(7×7) acquired with a negative bias applied *to the sample* and with a positive bias on the sample. Clear differences in the apparent height of many of the atoms are observed, which, as we shall see, arise from the energy-dependent changes in the density of states of the sample. Perhaps the most immediate conclusion that should be drawn from these observations is that it is common to interpret the features observed in scanning tunneling microscope images as "atoms." This superficial interpretation can often be misleading. A proper interpretation of scanning tunneling microscopy images requires an understanding of the tunneling mechanism together with some knowledge of the relevant variables (such as the density of states of sample and tip and the voltage-dependent tunneling probability) that determine the experimental result.

It is now widely recognized that the images obtained in STM are often strongly dependent on the sample–tip bias voltage in a nontrivial manner.[2-5] Although early STM studies focused on the application of STM as a microscope for observing topographic structure, the sensitivity to bias voltage also means that the STM is sensitive to the energy states of the sample and tip. This has two main implications: (1) tunneling microscopy does *not* reveal the positions of atoms themselves; and (2) using the STM, it is possible to obtain spectroscopic information with atomic spatial resolution.

Compared with other surface spectroscopy techniques such as ultraviolet photoemission spectroscopy (UPS), inverse photoemission spectroscopy (IPS), electron energy loss spectroscopy (EELS), and infrared reflection–absorption spectroscopy (IRRAS), the STM has a unique advantage. Whereas these other *techniques provide only information averaged over a large region of the surface*, the tunneling current in STM flows through a region only ≈ 5 Å in diameter,[6] so that spectroscopic information can be obtained on an *atom-by-atom* basis. This is an important advance, since many chemical and physical phenomena at surfaces are associated with "active sites" such as dopants, impurities, steps, or defects that occupy only a small fraction of the total surface area. Most experimental techniques average over a large surface area, making it difficult to study the properties of such local surface properties. With the STM, it is now possible to directly measure changes in electronic structure resulting from surface irregularities such as impurities, steps, and defects, as well as to examine the electronic structure of chemically inequivalent atoms in complex ordered structures such as the (7×7) reconstruction of Si(111).

The theory of tunneling in one dimension has received great attention and is well developed as a result of extensive studies performed using planar bulk tunnel junctions. (Several excellent books on both theoretical and experimental aspects of bulk tunneling phenomena are available.[7-9]) These theories of tunneling in bulk solids, together with more recent theoretical work (discussed in Chapter 2) specifically applied to the STM,[10-16] provide a suitable starting point for understanding tunneling spectroscopy from a theoretical standpoint. From a practical standpoint, there are many limitations on our ability to experimen-

tally measure and/or control the many variables affecting the tunneling process. Nevertheless, through careful experimental technique and an understanding of the factors that influence the tunneling, it is possible to glean much new information about the electronic structure of surfaces on a local scale. Here, we describe the experimental techniques commonly used for tunneling spectroscopy measurements, discuss the interpretation of the data, and point out some of the advantages and disadvantages of the experimental techniques. We also address the measurement of the tunneling barrier height, due to the importance of the tunneling transmission probability to the interpretation of tunneling spectroscopy results.

4.2 One-Dimensional Tunneling

Figure 4.2 shows an energy level diagram for the system consisting of the sample and tip that are separated by a vacuum. Here, the tip is considered to be a metal with a constant density of states, while the sample also contains a distribution of surface states as shown. When the sample and tip are independent, their vacuum levels are considered to be equal, as in Figure 4.2a., and their respective Fermi energies (or levels), E_F, lie below the vacuum level by their respective work functions Φ_s and Φ_t. The quantum-mechanical wavefunctions of the electrons are periodic in the solid and decay exponentially into the vacuum region like

$$\Psi = A \exp\left(- 2\sqrt{2m(\quad - E)}\, \frac{Z}{\hbar} \right), \tag{4.1}$$

where Z is the distance perpendicular to the surface plane and E is the energy measured with respect to the Fermi level. This energy-dependent decay of the functions wavefunctions is also illustrated in Figure 4.2a, for different states of the tip. More strongly bound electrons have large negative values for E and so decay quickly into the vacuum, while high energy states lying close to the vacuum level decay very slowly. The exponential decay of the wavefunctions into the vacuum is often written in terms of a "inverse decay length" K as $\Psi = A \exp(-KZ)$, where $K = 2\hbar H^{-1} \sqrt{2m(\quad - E)}$. If the sample and tip are in thermodynamic equilibrium their Fermi levels must be equal, as illustrated in Figure 4.2b. Electrons at tempting to pass from sample to tip (or vice versa) encounter a potential barrier, which is approximately trapezoidal in shape, but electrons can tunnel through if the barrier is sufficiently narrow.

When a voltage V is applied to the sample, its energy levels will be rigidly shifted upward or downward in energy by the amount $|eV|$, depending on whether the polarity is negative or positive, respectively. At positive sample bias, the net tunneling current arises from electrons that tunnel from the occupied states of the tip into unoccupied states of the sample, as in Figure 4.2c. At negative sample bias the situation is reversed, and electrons tunnel from occupied states of the sample into unoccupied states of the tip, as in Figure 4.2d. Since

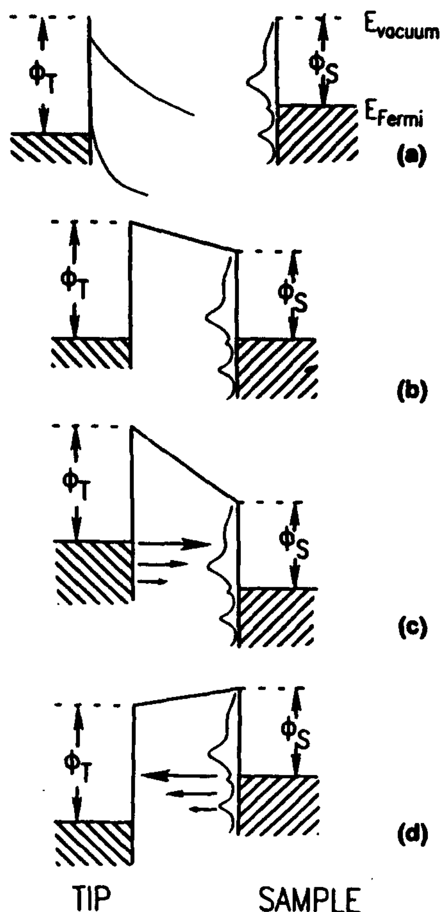

Figure 4.2 Energy level diagram of sample and tip: (a) separated sample and tip; (b) sample and tip in thermal equilibrium, without applied bias; (c) positive sample bias; (d) negative sample bias.

states with the highest energy have the longest decay lengths into the vacuum, most of the tunneling current arises from electrons lying near the Fermi level of the negative-biased electrode.

For any given lateral position of the tip above the sample (r), the tunneling current (I) is determined by the sample–tip separation (Z), the applied voltage (V), and the electronic structure of the sample and tip which is quantitatively described by their respective density of states $[(\rho(E)]$.

Spectroscopic information relies on changing the voltage V, but can be obtained in a number of ways depending on which of the other variables are

held constant and which are measured. Voltage-dependent STM imaging is the simplest way of obtaining spectroscopic information, by acquiring conventional STM "topographic" information at different applied voltages and comparing the results. More quantitative information regarding the symmetry properties and spatial localization of electronic states is obtained using modulation techniques to measure dI/dV (usually at constant average tunneling current) as a function of V, usually referred to as scanning tunneling spectroscopy or STS. More complete information can be obtained over a wider energy range simultaneously from complete I–V measurements, at the expense of considerably more complicated data acquisition electronics and data handling.

4.3 Voltage-Dependent STM Imaging

4.3.1 Experimental Technique

When a voltage V is applied to the sample (with the tip at ground), only those states lying between E_F and $E_F + eV$ contribute to the tunneling process. The sign and magnitude of the applied voltage, then, determine which states can contribute to the resulting topographic images. In many cases, conventional constant-current topographs (CCTs) show bias-dependent changes in appearance, which can be related to the spatial symmetry and energy of the surface electronic states. Such changes are most apparent on semiconductors[2, 3, 5, 17, 18] and semimetals such as graphite,[19] where the different electronic states are spatially separated and strongly localized.

One systematic method of identifying these bias-dependent changes is to acquire complete images at different bias voltages over the same nominal region of the surface. In this method, surface inhomogeneities such as point defects can be used as registration markers. For example, Figure 4.3 shows two sequential images of the Si(001) surface, obtained at negative and positive sample bias.[20] Here, naturally occurring point defects were used as alignment markers to ensure proper registration of the two complementary images. A close examination of Figure 4.3 shows that on the Si(001) surface there are two kinds of characteristic defects, each with its own unique electronic properties. Even on the nearly "perfect" regions, however, Figure 4.3a and b shows differences arising from the different local symmetry of the occupied and unoccupied states of the dimers comprising the ideal Si(001) surface.

A second method that is sometimes useful is to change the applied bias on a line-by-line basis during the raster-scanning of the tip, providing two (or more) interleaved images at different bias voltages. Although it seems that this method should provide better (and easier) registration of the images than the first method, in practice one must be careful to realize that as the bias voltage is changed, it is also possible for the spatial symmetry of the *tip* electronic states to change as well. This may also lead to shifts and distortions in the images that are different at different bias voltages, as demonstrated by

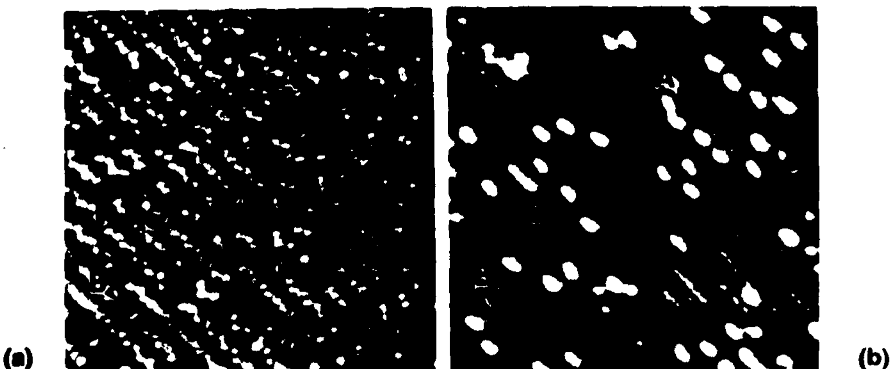

Figure 4.3 STM images of Si(001) surface with characteristic defects. **(a)** Image acquired at negative sample bias, tunneling from occupied surface states. **(b)** Image acquired at positive sample bias, tunneling into unoccupied surface states. (Reprinted with permission from Ref. [34].)

Tromp et al.[21] Such spatially separated, localized electronic states on the tip might be a result of the tip picking up some material from a semiconducting sample, either by accidental contact between sample and tip or through field-induced migration.

4.3.2 Interpretation of Voltage-Dependent STM Images

Under the assumptions that (1) the tip has uniform density of states, (2) the voltage is low (less than ≈ 10mV); (3) the temperature is low, and (4) only s-wave tip wave functions are important, the Tersoff–Hamann theory predicts that the tunneling current can be expressed as

$$I = 32\pi^3\hbar^{-1}e^2V\phi^2R^2\kappa^{-4}e^{2\kappa R}D_t(E_F)\rho(r_0,E_F), \tag{4.2}$$

where D_t is the density of states per unit volume of the tip, R is the tip radius, and $\rho(r_0,E_F)$ is the Fermi-level density of states of the sample, measured at the position corresponding to the center of curvature of the tip.

Under conditions of constant tunneling current, it can be seen from this formula that the contour followed by the tip is essentially a contour of constant Fermi-level density of states of the sample, measured at the center of curvature of the tip.

While the Tersoff–Hamann theory makes valuable contributions to the understanding of STM, the low-voltage approximation is often violated in practice, since many STM experiments are conducted at bias voltages of between 1 and 3 V. Under these conditions, the tunneling current arises from a *range* of states lying within eV of the Fermi level. For interpretation of such high-bias results, it becomes more useful to consider the predictions of simple

planar tunneling models, using the WKB approximation. The WKB theory predicts that the tunneling current is given by

$$I = \int_0^{eV} \rho_s(r,E)\rho_t(r, -eV + E)T(E,eV,r)\, dE, \quad (4.3)$$

where $\rho_s(r,E)$ and $\rho_t(r,E)$ are the density of states of the sample and tip at location r and the energy E, measured with respect to their individual Fermi levels. For negative sample bias, $eV<0$ and for positive sample bias, $eV>0$. The tunneling transmission probability $T(E,eV,r)$ for electrons with energy E and applied bias voltage V is given by

$$T(E,eV) = \exp\left\{ -\frac{2Z\sqrt{2m}}{\hbar} \sqrt{\frac{\Phi_s + \Phi_t}{2} + \frac{eV}{2} - E} \right\} \quad (4.4)$$

At constant tunneling current I, the contour followed by the tip is a relatively complicated function of the density of states of both sample and tip, together with the tunneling transmission probability. Despite the apparent complexity of the situation, several points should be remembered. First, examination of the transmission probability T shows that if $eV<0$ (i.e., negative sample bias), the transmission probability is largest for $E = 0$ (corresponding to electrons at the Fermi level of the sample). Similarly, if $eV>0$ (positive sample bias) the probability is largest for $E=eV$ (corresponding to electrons at the Fermi level of the tip). Thus, we see that the tunneling probability is always largest for electrons at the Fermi level of whichever electrode is negatively biased.

4.3.3 Applications of Voltage-Dependent STM Imaging

Elemental Semiconductors

In the case of ordered surfaces, voltage-dependent imaging can provide information on the relative spatial locations of the various electronic states at the surface. Some of the surfaces that have been extensively studied by this method include Si(001),[22-24] Ge(001),[25] Si(111)−(7×7),[2, 3, 26] the metastable cleaved Si(111)−(2×1) surface,[18, 27, 28] GaAs(110),[5, 29, 30] GaAs(100),[31, 32] and graphite.[19, 33]

Figure 4.4 schematically shows the atomic rearrangements involved in the reconstruction of the Si(001) surface. Figure 4.5 shows CCTs of the Si(001) surface obtained at negative and positive bias, reflecting the spatial distribution of filled and empty surface states, respectively. The geometric structure of this surface is well understood[24, 34-36] and consists of pairs of silicon atoms, each of which is bonded to two Si atoms in the next lower atomic layer and its dimer partner; the resulting (2×1) unit cell is outlined in Figure 4.5. At negative sample bias (Fig. 4.5a) the STM-CCT's show bean-shaped structures, while at positive sample bias (Fig. 4.5b) the images show a weak minimum between the dimer rows and a deep trough along the center of the dimer row. These differences can be seem more quantitatively in the corrugation profiles shows in Figure 4.6.

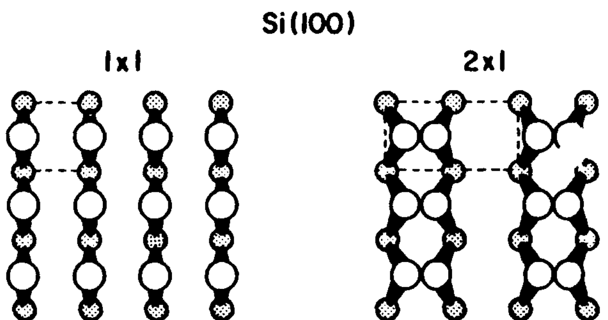

Figure 4.4 Schematic representation of the (2×1) reconstruction of the Si(001) surface, with the formation of two-atom dimers in the outmost layer of surface atoms.

These differences demonstrate a spatial separation of the filled and empty electronic states on the Si(001) surface.

These differences can be understood based on electronic structure calculations.[35,36] These show that the electronic structure of the dimers can be described in terms of a π-bonding state slightly below E_F, and a π-antibonding state slightly above E_F, with occupied σ and unoccupied σ^* states lying far from E_F, outside the energy range accessible by tunneling. The occupied π state predicted to be symmetric with respect to reflection through a mirror plane bisecting the dimer bond (A_1 symmetry), while the π^*-antibonding state is antisymmetric with respect to this reflection (B_1 symmetry) and therefore must have a *node* in the wavefunction at the center of the dimer bond.

The STM contours at negative bias reflect the contours of the occupied π state, while at positive bias the STM tip follows the contour of the empty π^* state. The deep trough observed in the positive-bias STM images corresponds to the location of the node in the wavefunction of the π^* antibonding state. Thus, the STM images directly reflect the spatial symmetry of these surface-state wavefunctions.

Changes in the spatial distribution of the surface-state wavefunctions can often be induced by species chemisorbed on the surface. Dosing the Si(001) surface with NH_3 significantly changes the negative-bias STM images, producing a slight depression in the center of the dimer bond, where images on the clean surface showed a maximum.[23, 34] These changes were atributed to hydrogen atoms produced by NH_3 dissociation interacting with the dimers. On the clean surface each surface Si atom is double-bonded via both a σ- and a π-bond to its dimer partner, while on the hydrogen-covered surface each surface Si atom is bonded via a single σ-bond to its dimer partner and via another σ-bond to a hydrogen atom. The changes in the negative-bias images induced by the reaction with NH_3 result from the different spatial distribution of the Si–Si π-state and the Si–H σ-state. Thus, the STM images alone can be used to distinguish dimers that have reacted with NH_3 from those which have not.[23, 34]

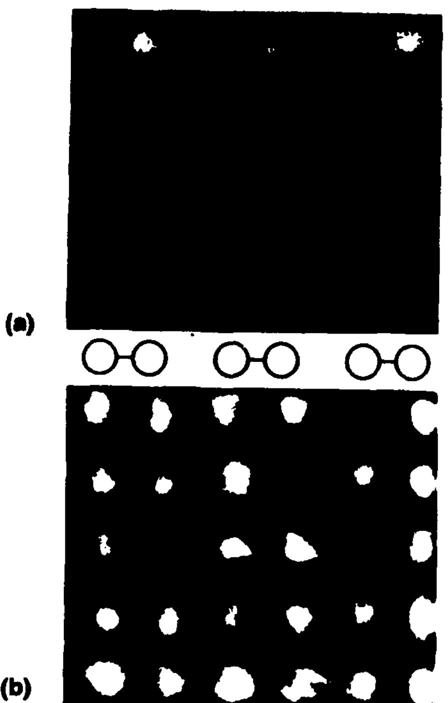

Figure 4.5 High-resolution image of Si(001) acquired at negative sample bias (a) and positive sample bias (b). At negative bias, electrons tunnel from an occupied π-state which has a maximum at the center of the Si-Si dimer bond. At positive bias, electrons tunnel into an empty π*-antibonding state, which has a node in the wavefunction at the center of the Si-Si dimer bond. (Reprinted with permission from Ref. [34].)

STM images of Si(111) surfaces are also strongly dependent on the bias voltage. The (2×1) reconstruction of the cleaved Si(111) surface[18, 28] shows a shift between negative- and positive-bias STM images due to the different spatial location of occupied and unoccupied electronic states. This shift provides strong confirmation for the π-bonded chain model proposed by Pandey.[37]

More complicated voltage dependence is observed for the Si(111)-(7×7) surface. This surface undergoes an extensive reconstruction extending several layers into the bulk, and the atomic arrangements have only recently been determined,[38] based in part on early STM results.[1] At most positive bias voltages, STM images reveal 12 adatoms of equal height in each unit cell, as shown in Figure 4.1b. In a narrow voltage range around +1.4 eV sample bias, the two triangular subunits in each unit cell appear to have slightly different heights. Differences between the two triangular subunits can be attributed to a [illegible] the stacking sequence of the underlying atomic planes [illegible] fault in one half, but not the other. The

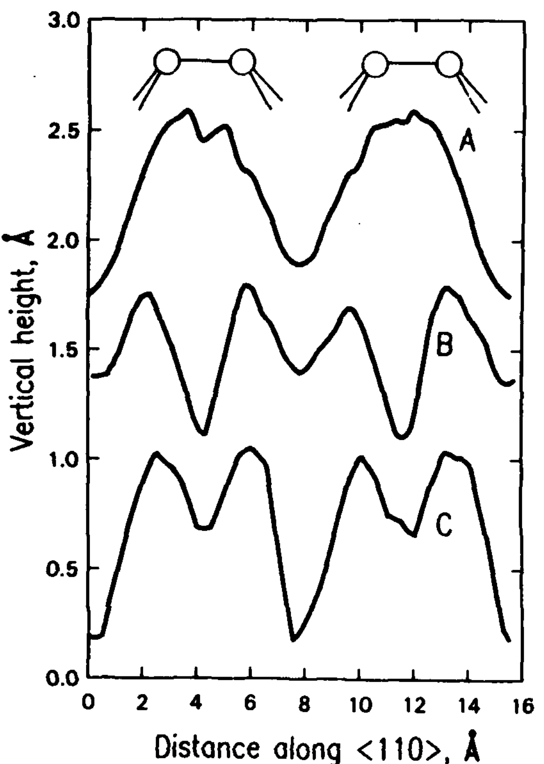

Figure 4.6 Differing appearance of the (2×1) reconstruction of Si(001): Corrugation profiles on Si(001) at negative (a) and positive bias (b), together with corrugation profile after dosing with NH_3; the symmetry in all three cases remains (2×1). (Reprinted with permission from Ref. [34].)

difference in stacking sequence leads to different interactions between the Si atoms in the first full atomic layer and those lying 4.6 Å below. Around +1.4 eV sample bias, the "unfaulted" half of the unit cell appears higher (indicating a higher density of states) than the faulted half. This situation reverses at negative sample bias voltages, as in Figure 4.1a, where the adatoms in the faulted half of the unit cell appear higher than those in the unfaulted half. Additionally, the adatoms nearest the deep corner holes appear higher than the central adatoms. These latest differences are attributed to the different environment of the corner adatoms (which are next to one dimer and one rest atom) and the central adatoms (which are next to two dimers and two rest atoms). Such voltage-dependent STM images,[3] together with local tunneling spectroscopy measurements to be discussed later[2, 22] have provided a great deal of insight into the electronic structure of this complicated reconstruction.

Compound Semiconductors

In compound semiconductors, voltage-dependent contrast changes can be directly related to charge transfer between surface atoms. The (110) surfaces of III–V semiconductors, such as GaAs(110), contain equal numbers of cations (Ga) and anions (As) in the surface layer; in GaAs, they are arranged in a chainlike structure. Charge transfer from Ga to As results in an occupied state centered at the As atoms and an empty state centered at the Ga atoms, and also results in a slight vertical displacement of the Ga atoms with respect to the As atoms. STM images[5] reveal a shift between the peaks observed at positive and negative bias. The peaks at negative bias correspond to the positions of the As atoms, and those at positive bias reveal the Ga atoms. A comparison of this bias-dependent shift with theoretical calculations also allowed the tilt angle between Ga and As atoms at the surface to be quantitatively determined.[5,39]

Pashley et al.[40,41] investigated (100) and (111) surfaces of GaAs initially grown by molecular beam epitaxy and capped with a protective layer or arsenic, which were then cleaned by thermal annealing under ultrahigh vacuum conditions. The (100) and (111) surfaces exhibit a rich variety of structure due to the variable stoichiometry of the surface layers. Biegelsen et al.[31,32] studied these same surface directly grown by *in situ* molecular beam epitaxy. The *in situ* preparation allows the stoichiometry to be carefully controlled and generally results in more highly ordered surfaces.

Adsorbates and Impurities

Voltage-dependent STM imaging is not restricted to ordered surfaces as above, but is also very useful for identifying and studying the properties of impurities and defects at surfaces. On semiconductor surfaces, local charging due to adsorbates[30,42] and defects[43] can shift the surface-state bands with respect to the Fermi level, resulting in apparent height changes, which correspond to the electrostatic screening length. For strongly charged adsorbates and/or lightly doped semiconductors, these effects can dominate the appearance of defects, as in the case of oxygen on n-type GaAs(110).[42] Adsorbates on metals and covalently bonded adsorbates on semiconductors give rise to local changes in the surface electronic structure that allow them to be imaged.

The ability to differentiate between chemically inequivalent atoms is demonstrated in Figures 4.7 and 4.8. Figure 4.7 schematically shows the atomic configuration; the surface consists of a bulk-like (111) surface of Si, with a random distribution of aluminum and silicon adatoms. Figure 4.8 shows the STM images at positive (4.8a, + 1.2 V) and negative (4.8b, −1.2 V) bias.[43] At positive bias (4.8a) each bright protrusion in the ordered structure is an Al adatom. In many of the locations where an Al adatoms would be expected, the unit cell appears darker but still has a protrusion in the center. These darker unit cells consist of Si adatoms, rather than the expected Al adatoms, situated

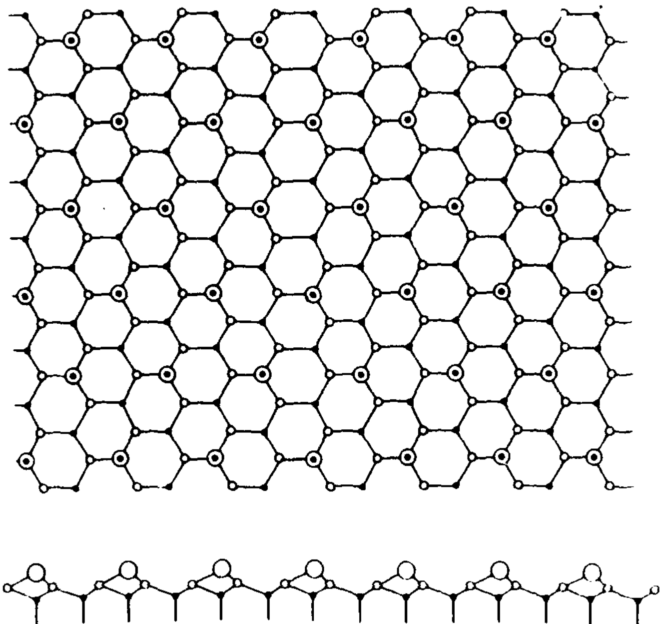

Figure 4.7 Schematic illustration of $(\sqrt{3} \times \sqrt{3})$ reconstruction of Al/Si(111); Al adatoms sit in "T_4" sites atop a bulk-like Si(111) lattice.

atop a bulk-like Si(111) surface. Switching the bias to −2 eV causes the contrast to reverse so that the Si adatoms appear higher ≈ 1 Å higher than the Al adatoms. By choosing the bias polarity, then, either the Al adatoms or the Si adatoms can be selectively imaged. The origin of these contrast changes is revealed from theoretical calculations,[44] which show that the Al adatoms have an unoccupied p_z orbital, which in Si is shifted below E_F. These changes in the state density directly give rise to contrast in the STM constant-current topographs.

Arsenic-terminated Si(111) and Si(100 surfaces have proven to be very interesting systems as well, and has been the subject of several studies by Becker and co-workers.[45,46] A number of other systems have also been studied by voltage-dependent STM imaging. On graphite, interactions of the surface carbon atoms with those in deeper layers lead to two kinds of inequivalent carbon atoms in the surface layer, producing interesting voltage-dependent tunneling behavior.[19,33,47] Metal overlayers on semiconductors have also proven to provide rich voltage-dependent structure; those studied include Ag/Si(111),[48] Al/Si(111),[49] and Cu/Si(111).[50] Most of these metal-on-silicon systems show strongly voltage-dependent changes in constant-current STM topography resulting from complex electronic structure. For such systems, an understanding of the dependence of the STM images on applied

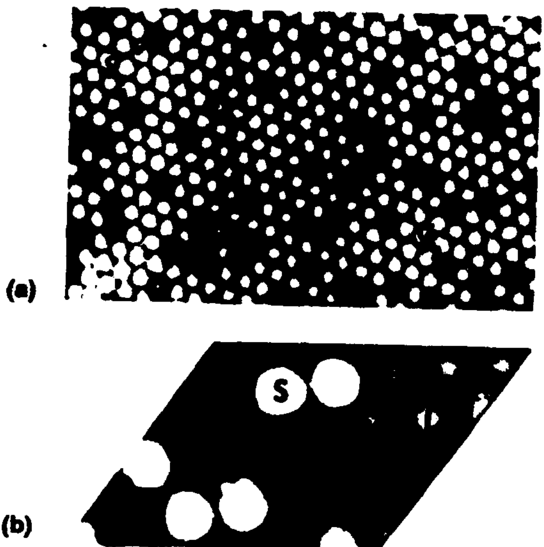

Figure 4.8 STM images of partial ($\sqrt{3} \times \sqrt{3}$) reconstruction of Al/Si(111) at positive (a) and negative (b) bias, demonstrating "atom-selective imaging." The ($\sqrt{3} \times \sqrt{3}$) overlayer is incomplete, so that half the surface atoms are aluminum adatoms (as in Fig. 4.7) and half are silicon adatoms. In a, bright atoms are Al adatoms and dark atoms are Si; in b, the situation is reversed—Si atoms appear bright and Al atoms appear dark. (Reprinted with permission from Ref. [49].)

bias is crucial for understanding the atomic features which give rise to the STM "topographic" structure.

4.4 Modulation Techniques: STM

Constant-current topographs often reveal electronic structure information, but separating the contributions of electronic and geometric structure is not straightforward. One way of obtaining quantitative spectroscopic information in the STM is the use of modulation techniques.

4.4.1 Experimental Techniques

The most common modulation technique is the scanning tunneling spectroscopy, or STS technique first used by Binnig and Rohrer.[17,51] The STS technique involves superimposing a small high-frequency sinusoidal modulation voltage $V_{mod}\omega_{mod}$ on top of the constant DC bias V_{DC} between sample and tip. The AC component of the tunneling current is measured with a lock-in amplifier, with the in-phase component directly giving $dI/dV|_{V=V_{DC}}$ simultaneously with the

sample topography. To probe the density of states as a function of energy with this technique, the lock-in output is measured as a function V_{DC}. The modulation frequency ω_{mod} must be faster than the closed-loop bandwidth of the STM feedback system (typically 1–2 kHz). If the modulation frequency is too low, the feedback control electronic will attempts to compensate for the applied modulation by changing the gap spacing. As the frequency is increased the sample-tip capacitance contributes an additional *displacement* current 90° out-of-phase with the applied modulation, which becomes larger as the modulation frequency is increased. In practice, the optimal modulation frequency is slightly above the cutoff frequency of the feedback loop and can be found can be found by identifying the frequency range where the induced modulation dI/dV is independent of frequency.

4.4.2 Interpretation

High Voltage: Barrier State Spectroscopy

When the applied DC bias V_{DC} is larger than the work functions of sample and tip, structure in dI/dV arises primarily from field, or barrier states.[17,26,52] These states arise from the interaction between the surface electrons and the polarization they induce in the bulk. The interaction traps the electron in the near-surface region while leaving it free to translate parallel to the surface.[53] These states are essentially standing-wave states formed between the sample and the potential barrier between sample and tip, and their energy depends on the shape of the tunneling barrier. The oscillatory electron wavefunctions lead to constructive or destructive interference depending on the phase-matching conditions at the boundary. Since the shape of the boundary is determined in part by the applied voltage, changing the voltage causes the wavefunctions to alternate between constructive and destructive interference, leading to oscillations in the tunneling probability. Binnig et al.[17] first observed these barrier resonances, using a gold tip on a Ni(100) surface. Becker et al.[26] performed similar studies on tungsten surfaces and showed that through a numerical integration of Schrodinger's equation, the oscillations in dI/dV could be used to determine an *absolute* sample–tip separation, which is very difficult to determine otherwise.

Low Voltages: Surface State Spectroscopy

At lower bias voltages, (when V_{DC} is lower than the sample and tip work functions) structure in dI/dV as a function of V_{DC} is associated with the surface density of states. Structure in the surface density of states can arise from critical points in the surface-projected bulk band structure or it may arise from from true surface states, which are generally associated with surface reconstructions. The interpretation of these low-bias dI/dV measurements is generally based on the WKB approximation for the tunneling current, given as Eq. (4.3). Differentiating that equation gives

$$\frac{dI}{dV} = \rho_s(r,eV)\rho_t(r,0)T(eV,eV,r) + \int_0^{eV} \rho_s(r,E)\rho_t(r,E-eV)\frac{dT(E,eV,r)}{dV}\,dE. \quad (4.5)$$

The first term in Eq. (4.5) is the product of the density of states of the sample, the density of states of the tip, and the tunneling transmission probability T. The second term contains the voltage dependence of the tunneling transmission factor.

While the tunneling transmission probability T is usually unknown, inspection of Eq. (4.4) shows that it is a smooth, monotonically increasing function of the applied voltage V. Thus, at any fixed location the voltage dependence of the tunneling transmission probability contributes a smooth background on which the spectroscopic information is superimposed. Because the increase is smooth and monotonic, structure in dI/dV as a function of V can usually be assigned to changes in the state density via the first term of Eq. (4.5). As a result, these measurements can provide a measure of the density of states as a function of energy at any particular location on the surface.

Often, one measures dI/dV at some fixed energy simultaneously with the sample topography, resulting in an "image" of dI/dV. Changes in dI/dV can be produced by localized electronic states or by changes in the transmission probability. Additionally, there is yet another complicating contribution of "topographic" origin. Consider the state density contours depicted in Figure 4.9. According to the Tersoff–Hamann theory,[11,12] the tip is expected to follow a contour of constant state density. At vertical separations that are large compared to the distance between the individual atoms on the surface, the atomic corrugations die away and the sample becomes laterally isotropic. For this to occur, the effective decay length of the wavefunctions above a local "peak" in the topography (κ_p-1) must be shorter than those above a local "valley" (κ_v-1).

This effect can be seen more quantitatively using an approximation given by Tersoff[11] for the Z-dependent corrugation $\Delta(Z)$,

$$\Delta(Z) \simeq \frac{2}{\kappa}\exp\left(-\frac{\pi^2 Z}{a^2\kappa}\right) \quad (4.6)$$

where a is the lattice constant and κ is the average inverse decay length. A simple analysis based on this formula leads to the approximate expression;

$$\kappa_v \simeq \kappa_p - \frac{2\pi^2}{a^2\kappa}\exp\left(-\frac{\pi^2 \bar{Z}}{\kappa a^2}\right) \quad (4.7)$$

All other factors being equal, the effective decay length (and the tunneling transmission factor T) will be greater when measured at a location corresponding to a valley in the topography than when measured over a peak. This spatial variation in the transmission probability shows up in measurements of dI/dV as

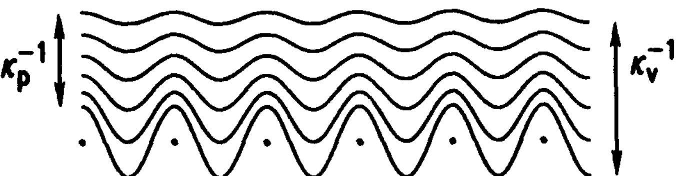

Figure 4.9 Exponential decay of equipotential contours for a corrugated surface. The contours decay more quickly above a protrusion than above a depression.

a background which is essentially an "inverted" topography. Thus, images showing the spatial variation of dI/dV obtained under conditions of constant average tunneling current always contain some topographic information convoluted in with the electronic information.

STS measurements of dI/dV at constant average tunneling current also contain a strongly voltage-dependent background whose origin can be seen by first writing the tunneling current as

$$I = \int_0^{eV} \rho_s(r,E)\rho_t(r,E-eV)\exp\left[-\frac{2\sqrt{2m}Z}{\hbar}\sqrt{\phi + \frac{eV}{2} - E}\right]dE. \quad (4.8)$$

For simplicity, we can assume that the density of states ρ is constant for both sample and tip. Then, neglecting the influence of the applied voltage on the tunneling barrier (a valid assumption for $eV << \phi$) the derivative dI/dV is given by

$$\frac{dI}{dV} = e\rho_s\rho_t\exp\left(-A\sqrt{\phi - \frac{eV}{2}}\right)Z \quad (4.9)$$

where $A = 2\hbar^{-1}\sqrt{2m}$. In modulation experiments conducted under conditions of average constant average tunneling current the sample–tip separation Z increases as the DC voltage $\bar{V}$ is increased; this variation in Z must be explicitly included. In the low-bias limit, Eq. (4.8) reduces to

$$\bar{I} = \rho_s\rho_t\bar{V}\exp(-A\sqrt{\phi}Z). \quad (4.10)$$

Solving this for Z and substituting the result into Eq. (4.9) gives $dI/dV = \bar{I}/\bar{V}$. Under conditions of constant average tunneling current $\bar{I}$, the quantity dI/dV diverges like $1/V$ as V approaches zero and presents a background term on which the desired spectroscopic information is superimposed.

The $1/V$ divergence problem can be significantly improved by instead operating under conditions of constant *resistance*. This type of operation was first utilized by Kaiser and Jaklevic[54] to observe surface states on clean Au(111) and Pd(111) surfaces. On these most of the variation in the surface density of states arises from critical points in the bulk density of states. This can be seen in Figure 4.10 which shows Kaiser and Jaklevic's constant-resistance dI/dV spectra for Pd(111) (Fig. 4.10A), together with the projected bulk band structure (Fig.

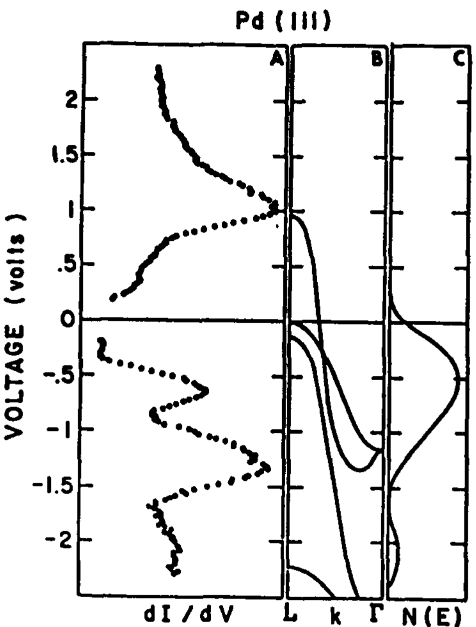

Figure 4.10 Tunneling spectroscopy data on Pd(111) surface obtained by Kaiser and Jaklevic under conditions of constant resistance, compared with the bulk band structure projected onto the (111) surface. Most of the features observed in the tunneling spectroscopy correspond with critical points in the bulk-projected band structure, where the density of states is expected to be high. (Reprinted with permission from Ref. [54].)

4.10B) and the results of ultraviolet photoemission spectroscopy measurements (Fig. 4.10C). The peaks near +1.0 and −1.3 V in dI/dV closely correspond with critical points in the 2-D projected band structure, while the dI/dV peak near −0.6 eV is in reasonable agreement with a surface state observed in photoemission measurements. At constant average tunneling current, this information would likely have been obscured by the $1/V$ background.

4.4.3 Experimental Applications of STS

The modulation-based STS technique has been widely applied. Garcia and co-workers[52, 55] first applied it to clean and oxidized Ni(100) surfaces, where they observed barrier resonances at high voltages but also found evidence for true surface states at lower voltages. Salvan et al.[56] applied this technique to the $(\sqrt{3} \times \sqrt{3})R30°$ overlayer of Au on Si(111) and observed a strong peak near 1 eV above E_F associated with a surface states, as well as field emission resonances at higher voltages. Becker et al.[57] applied this technique to the famous (7×7) reconstruction of Si(111) and found two unoccupied surface states, at +1.5 and

+2.8 eV above E_F, and also observed difference between the energy of the 1.5 eV surface state between the faulted and unfaulted halves of the unit cell. In later work,[58] they applied STS to the study of surface states on various alloys of Si, Ge, and Sn and observed structure in dI/dV associated with the surface states of these alloys. Other STS studies have investigated the electronic structure of GaSe[59] and stepped Ni(111)/H[60] surfaces.

Although the standard STS technique is relatively simple to apply, many of the published studies have demonstrated two important disadvantages to the standard STS technique, as conventionally applied at constant average tunneling current. The first is the $1/V$ dependence of dI/dV, which makes it difficult to observe structure at low voltages. The second (and more severe) limitation is that at lower voltages, the tip moves toward the surface in order to maintain constant tunneling current; if the density of states is too low, the tip will crash into the surface. Becker[57, 58] has shown the tip displacement vs. voltage at constant tunneling current for Si(111)-(7×7). For comparatively large bias voltages the displacement presents no insurmountable problem; however, it can restrict the ability to perform measurements at lower voltages. This effect is particularly dramatic on semiconductor surfaces, since then the density of states near the Fermi level is typically low and the tip must push in even closer to the surface to draw the demanded tunneling current at low voltages. Since the electronic structure near the Fermi level is often of particular interest on semiconductors, this may be a significant limitation. In the case of conductors and superconductors, however, it does not always present a difficulty. The STS technique works well in cases where states lying near E_F are not of primary interest, but cannot probe electronic structure near the Fermi level. As in the case of voltage-dependent STM imaging, a complete mapping of the surface electronic structure as a function of energy and position requires many repeated measurements over the same area. This procedure is tedious at best, and is often unsuccessful due to instability in the tip as well as thermal drifts in the microscope.

4.5 Local *I–V* Measurements

Tunneling spectroscopy data can be simultaneously obtained over a wider range of applied voltages by acquiring complete curves of I vs. V, and later analyzing the results. This is the approach taken in early work by Feenstra et al.[28] on the Si(111)-(2×1) surface. In such early studies, blunt tips were used and it was not possible to accurately establish the tip position. To take full advantage of the spatial resolution of the STM, the $I–V$ curves need to be measured with "atomic" resolution and at well-defined locations on the surface to be able to correlate the surface "topography" with the local electronic structure. Since the tunneling probability is also affected by the sample–tip separation, such a measurement is also best performed at a fixed sample–tip separation. As shown by Hamers et al.,[2] this can be achieved by synchronizing the electronics such that the feedback loop is opened for only short periods of time, with the result that the $I–V$ curves

and the conventional "topography" information can be obtained simultaneously while the tip is slowly scanning across the surface, as schematically illustrated in Figure 4.11.

4.5.1 Experimental Methods

Several methods of acquiring such local I–V information are available. These methods differ primarily in the details of the data acquisition hardware, but all provide essentially identical information. Atomically resolved I–V measurements were first performed by Hamers et al.[2] by rapidly acquiring I–V curves (each at a fixed sample–tip separation) while simultaneously slowly scanning the tip position. This technique was used to map out the complete electronic structure of the Si(111)-(7×7) unit cell. The method is denoted current imaging tunneling spectroscopy (CITS) because in addition to the conventional image of the surface height as a function of position, I–V spectroscopy information is also obtained at each location, thereby permitting the local electronic characteristics to be directly imaged from the current measurements.

In the CITS method, a sample-and-hold circuit is installed in the feedback controller to gate the feedback control system on and off. The gating circuit usually consists of a commercial sample-and-hold amplifier, which can be located before, after, or within the feedback controller. The timing of the electronics is depicted in Figure 4.12. Typically, the period of the waveform is approximately 500 μsec, during which time approximately 80 μsec is devoted

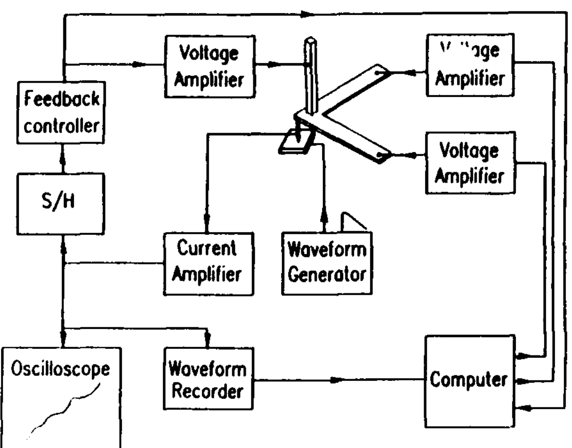

Figure 4.11 [illegible] setup for local I–V spectroscopy. The feedback loop [illegible] amplifier (or equivalent). The tunneling I–V [illegible] recorder and stored in the computer while the tip [illegible]

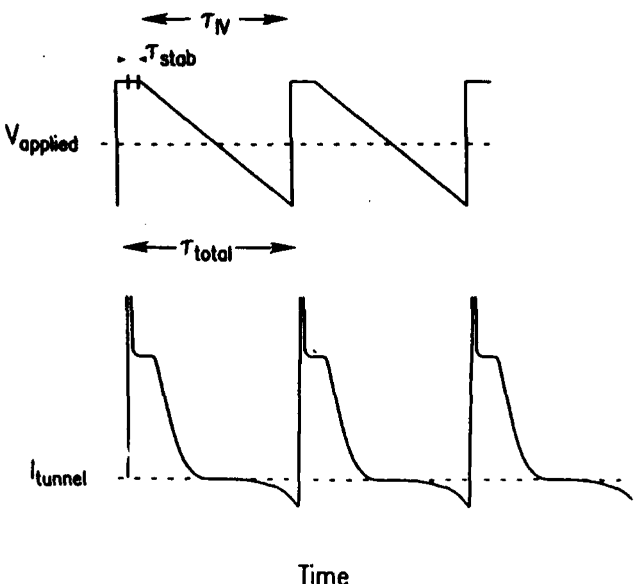

Figure 4.12 Timing diagram for rapidly multiplexed tunneling spectroscopy measurements, allowing sample topography and tunneling I–V curve to be measured at each position on the surface.

to stabilizing the sample-tip separation, 400 μsec is devoted to the tunneling I–V curve, and the remaining 20 μsec is "dead time," which allows for capacitive transients to die out. When the feedback system is active, a constant voltage V_{stab} is applied to the sample, and the feedback control adjusts the tip height to maintain a constant tunneling current. When the feedback system is deactivated by means of the sample-and-hold circuit, it no longer corrects for changes in the tunneling current but instead keeps the tip fixed. The applied voltage is then linearly ramped between two voltages, and the tunneling I–V curve is measured. The applied voltage is finally returned to the value V_{stab}, and the feedback controller reactivated. By acquiring the I–V curves rapidly compared to the scan speed of the tip, both the sample "topography" and spatially resolved tunneling I–V characteristics are measured at each location in a two-dimensional raster scan over the surface. The high speed eliminates both vertical and lateral drift of the tip position, providing a one-to-one correspondence between each point in the topography and an I–V curve.

In practice, many modifications of this technique are possible.[28,29,61,62] The I–V curves can be measured using waveform recorders, digital oscilloscopes, or analog-to-digital converters in the computer itself. Likewise, the generation of the bias waveform and the timing can be controlled externally or internally to the computer. The I–V curves may also be measured at each surface location or

only at a few selected locations. Despite these differences, the various methods generally provide the same essential information: measurement of I as a function of V at constant sample–tip separation at known locations on the surface.

One major experimental difficulty with obtaining constant-separation I–V curves is that a wide dynamic range of current measurement is required, since the current varies almost exponentially with the applied voltage. In practice, this creates limitations in the ability to obtain electronic information over a wide voltage range at constant separation. One way around this is to allow the gap spacing to change in a measured, controlled manner, and then correcting the tunneling current for this change in sample–tip separation using the known tunneling barrier height (which is directly related to the inverse decay length). Using this idea, Feenstra and Stroscio[63] measured I–V spectra on GaAs(100), which, when corrected for changes in sample–tip separation, effectively corresponded to performing measurements over eight orders of magnitude in tunneling current. Such measurements at variable sample–tip separation require measuring *both* the tunneling current *and* the sample–tip separation as a function of V, and also require measuring the tunneling barrier height to determine the decay rate of the wavefunctions in the vacuum.

The stabilization voltage V_{stab} plays a special role by determining the contour that the tip follows as it scans across the surface, and usually must be chosen arbitrarily. The choice of V_{stab} affects the spatially dependent I–V curves, since the sample–tip separation may be different at each location. Berghaus et al.[64] and Feenstra[28] explicitly demonstrated the changes in local I–V spectra on Si(111)-(7×7) and Si(111)-(2×1) surfaces at different stabilization voltages. Fortunately, the influence of the choice of stabilization voltage can be almost completely eliminated by proper normalization of the spectroscopy data to eliminate the Z-dependence, using a normalization procedure suggested by Feenstra.[28] This normalization procedure will be discussed in more detail below.

4.5.2 Analysis and Interpretation of I–V Data

Analysis of the I–V information can be performed in a number of ways. For example, the tunneling current I resulting from some bias voltage V can be directly imaged—a "current image." These images are dependent on the contour that the tip follows, and so cannot be directly interpreted in a quantitative fashion. However, the *symmetry* of the images provides information about the different spatial symmetry of the electronic states of the surface. For example Figure 4.13 shows current images on Si(111)-(7×7) at various bias voltages between +2 and −2 V. Distinct changes in the *symmetry* of the images occur at −0.8 and +1.4 V. As we shall see, more detailed analysis of the tunneling spectroscopy data shows that these changes in symmetry correspond to energies at which surface states are observed. The degree to which the choice of stabilization voltage influences the CITS images can be easily assessed by comparing

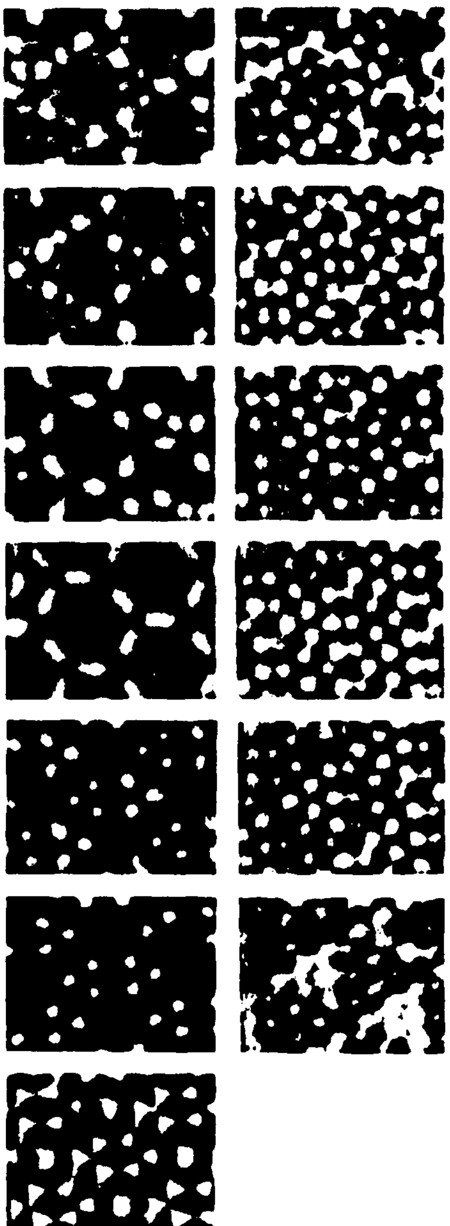

Figure 4.13 Images showing the spatial distribution of tunneling current in the Si(111)-(7×7) unit cell as a function of applied bias. Although difficult to interpret directly, such "current images" show pronounced changes in symmetry at particular voltages (near −0.8 and + 1.4 eV, for example), which can be related to the symmetry of the surface states contributing to tunneling. (Reprinted with permission from Ref. [22].)

data acquired at different stabilization voltages. On the Si(001) surface, Hamers et al.[22] showed the equivalent information was obtained either at negative or positive sample bias. On Si(111)-(7×7), changes in the symmetry of the current images coincided with the energies at which steep increases were observed in the local conductance and also coincided with the energies of the surface states known from photoemission studies.[2,65,66] In some other cases, however, changes in the tunneling probability can dominate the electronic structure information,[18,64] particularly if the energy does not correspond to the energy of a known surface state. In any case, interpretation of the CITS images must be done carefully and must be corroborated by studying the I–V curves at selected locations or by normalizing the data to remove the Z-dependence, as will be discussed below.

Identifying the surface-state energies is usually done by analyzed the I–V curves only at selected locations or averaged over a large region. Figure 4.14a shows plots of the conductance (I/V) vs. V measured at different specific locations within the Si(111)-(7×7) unit cell, together with the surface states observed in ultraviolet photoemission[65] and inverse photoemission[66] spectroscopies. The conductance curves in Figure 4.14a show steep "onsets" at particular voltages corresponding to the energies of the surface states. The energies of these onsets correspond exactly with the energies of the surface states determined by photoemission shown in Figure 4.14b, and also correspond to the energies at which symmetry changes are observed in current images. The atomically resolved tunneling spectroscopy measurements directly reveal the atomic origins of the various electronic states. The states near −0.35 and +0.5 eV arise from the 12 adatoms within each unit cell, while the state near −0.8 eV arises from the 6 "rest" atoms. The states near −0.35 and +1.4 eV also appear to have some contribution from underlying layers, since they show an asymmetry between the faulted and unfaulted halves of the (7×7) unit cell.

Since dI/dV is small except at the "onset" energies, spatial maps of dI/dV at these energies can be loosely interpreted as "images" of the surface states themselves. However, just as in modulation experiments, the spatial maps of dI/dV also contain a background contribution in the form of an "inverted topography." Only when dI/dV is large and corresponds to the energy of a surface state can surface states be imaged in this way. This is the case, for example, in the surface-state images of Si(111)-(7×7),[2] where images of dI/dV were presented only at energies where the rapid increase in dI/dV overwhelmed this background effect.

Extracting quantitative information about the sample density of states is difficult because the density of the states of the tip ρ_t and voltage-dependent tunneling transmission probability $T(E,eV)$ are almost always unknown. This can create confusion when comparing spectroscopy results obtained at different lateral positions, since the sample–tip separation (and consequently, the transmission probability) is dependent on the contour that the tip follows, which is determined by the feedback stabilization voltage V_{stab}. The voltage

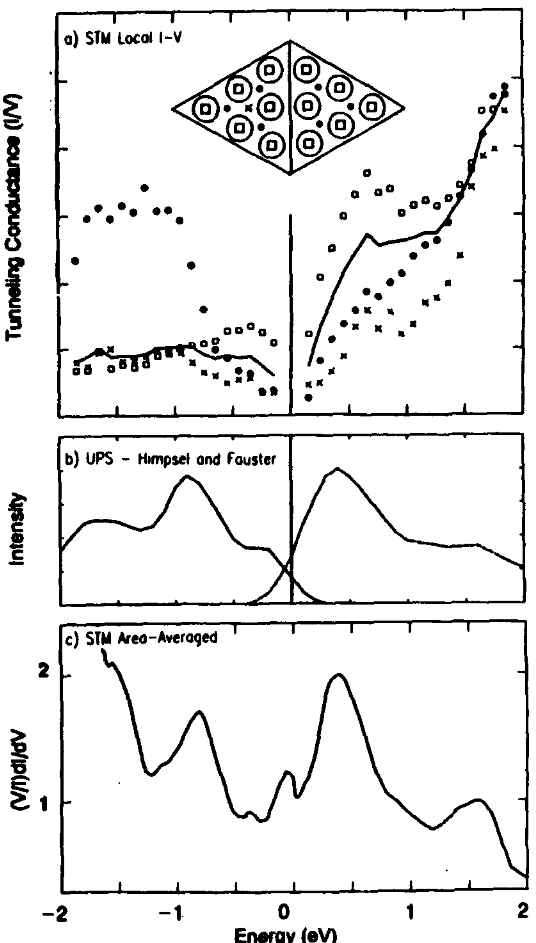

Figure 4.14 Spatially localized tunneling spectra on Si(111)-(7×7) surface (a), compared with photoemission/inverse photoemission spectra of Himpsel and Fauster (Reprinted with permission from Refs. [65 and 66]) (b), and "normalized" tunneling spectra area-averaged over entire (7×7) unit cell (c). (Reprinted with permisssion from Ref. [43].)

dependence of the transmission probability may also vary as a function of position due to variations in the local work function, band-bending effects, and other phenomena.

In the case of superconductors, the energy range of interest is small enough that the voltage dependence of the tunneling barrier is only a minor effect. In the study of surface states of metals and semiconductors, however, the energy range of interest usually extends several eV on either side of E_F. Nevertheless,

since $T(E,eV)$ is a slowly varying function, semiquantitative electronic structure information can still be obtained and is useful to consider.

Dividing both sides of Eq. (4.3) by the static conductivity I/V, and then dividing both numerator and denominator by the factor $T(eV,eV)$ gives

$$\frac{dI/dV}{I/V} = \frac{\rho_s(eV)\rho_t(0) + \int_0^{eV}\left[\frac{\rho_s(E)\rho_t(E-eV)}{T(eV,eV)}\right]\left[\frac{dT(E,eV)}{dV}\right]dE}{\left(\frac{1}{eV}\right)\int_0^{eV}\rho_s(E)\rho_t(E-eV)\left[\frac{T(E,eV)}{T(eV,eV)}\right]dE} \quad (4.11)$$

Feenstra[28] has argued that since $T(eV,eV)$ and $T(E,eV)$ appear as ratios in the second term in the numerator and in the denominator, their dependences on separation and applied voltage tend to cancel. Thus, this normalization effectively reduces the data to a form like

$$\frac{dI/dV}{I/V} = \frac{d(\log I)}{d(\log V)} = \frac{\rho_s(eV)\rho_t(0) + A(V)}{B(V)} \quad (4.12)$$

This quantity is equal to unity at $V = 0$. Assuming that $A(V)$ and $B(V)$ vary slowly with voltage, this provides a convenient normalization. Figure 4.14c shows the results of this analysis for area-averaged tunneling I–V data for Si(111)-(7×7).[67] A comparison of this curve with the atomic-resolution conductivity measurements in Figure 4.14a and the photoemission results in Figure 4.14c shows a close correspondence, with surface-state peaks occurring at −1.5, −0.8, −0.2, +0.45, and +1.55 eV. Surprisingly, even the relative intensities of the tunneling data and the photoemission data appear in be similar, except for the state near −1.5, which appears quite small in the tunneling data.

One major advantage of this normalization procedure is that it tends to eliminate the distance dependence of the tunneling probability. Feenstra et al.[28] acquired I–V curves at different sample–tip separations on Si(111)-(2×1) and verified that this normalization minimizes the influence of the sample–tip separation Z, as shown in Figure 4.15. The second panel of this figure shows normalized Si(111)-(2×1) tunneling spectra measured at five different sample–tip separations (indicated by open triangles, filled triangles, open squares, filled squares, and filled circles). The normalized data overlay one another, demonstrating that the normalization procedure minimizes the effect of changing sample–tip separation. A comparison of this data with predictions of the electronic structure based on Pandey's Π-bonded chain model is shown in the third panel, demonstrating good agreement between the experiment and theory for this particular model. Similar results have been obtained by Kuk and Silverman[68] on Au(100) surfaces.

While calculating $d(\log I)/d(\log V)$ provides a *convenient* normalization, a number of researchers have incorrectly stated that this "tunneling density of states" is proportional to the true density of states. This is certainly not true. First, simple calculus shows that since the tunneling current is a *continuous*

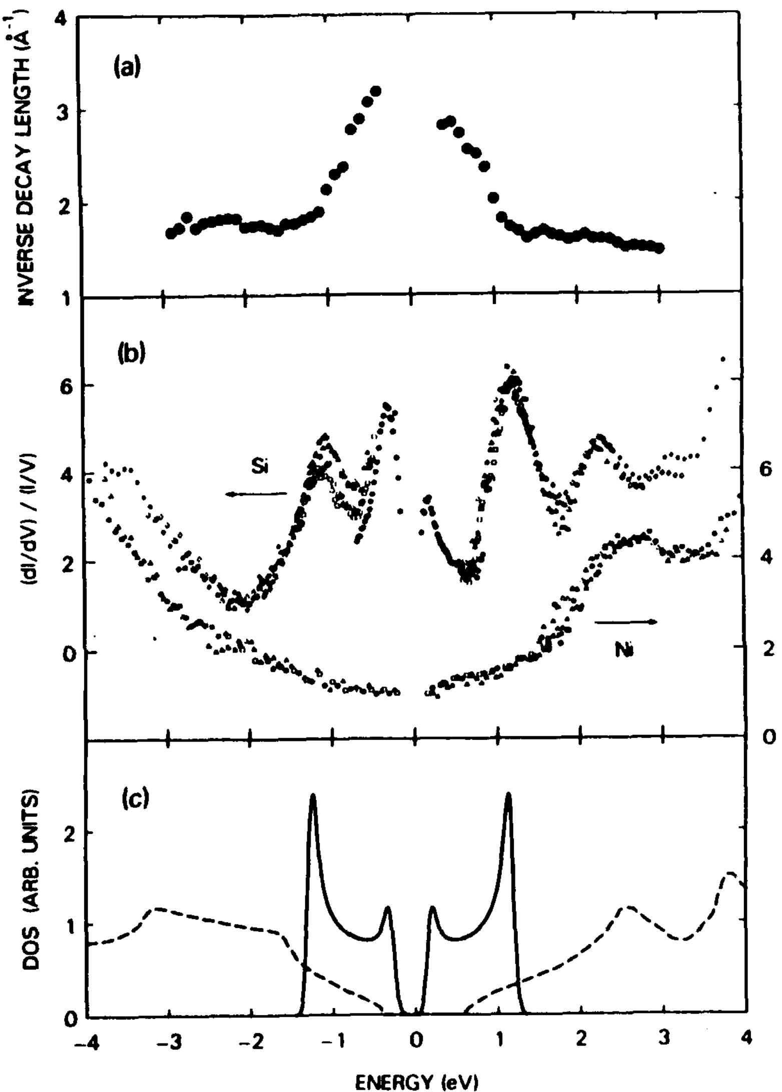

Figure 4.15 Tunneling spectra on Si(111)-(2×1) surface. **(a)** Inverse decay length as a function of applied bias. **(b)** Normalized tunneling spectra on Si(111)-(2×1) acquired at a number of different sample–tip separations, along with spectra measured on a Ni film. **(c)** Calculated density of surface (solid line) and bulk (dotted line) states for the π-bonded chain model of Pandey. (Reprinted with permission from Ref. [28].)

function of the applied voltage, then $\frac{dI/dV}{I/V}$, or equivalently, $\frac{d \log I}{d \log V}$ must equal unity at $V=0$. Thus, the above procedure tends to normalize the spectra by the density of states at the Fermi level, which will be different at different locations on the surface. Additionally, numerical calculations below show that relative intensities of the peaks in such normalized tunneling spectra show significant variations from those in the actual state density. The origin of these quantitative differences in peak heights can be easily understood and will be discussed below.

The main goal of the $(dI/dV)/(I/V)$ "normalization" is to attempt to minimize the effect of the voltage dependence of the tunneling barrier. For gapless surfaces where the entire I–V curve can be approximated by a simple exponential function of V, the normalization works well. If there is a surface-state bandgap, however, then the pseudoconstants $A(V)$ and $B(V)$ in Eq. (4.12) change rapidly at the band edges. This leads to artificial discontinuities in the data that are not realistic. A more accurate procedure in such cases is to fit the entire I–V curve (including regions well outside the surface-state bandgap) to an exponential function. In the presence of a surface-state gap, this fitted I–V curve more accurately represents the smoothly increasing tunneling transmission probability than the experimental one does. Thus, the best procedure is to calculate (dI/dV) from the experimental data, and then to divide this by the fitted I–V curve.

Thus, while the $(dI/dV)/(I/V)$ profiles a *convenient* normalization of the tunneling spectroscopy data, this normalization is not correct in all situations and great care must be made in any quantitative comparisons, particularly for curves that show significant deviations from a simple exponential dependence.

4.5.3 Comparison of Normalized I–V Data with True DOS

Numerical Integration of Tunneling Equations

To show how the tunneling spectra resulting from this normalization compare with the local state density, an artificial density of states function has been created and then, using Simmons' formulas[69] (which also includes effects of the image potential), numerically integrated to obtain the I–V curve predicted from tunneling theory. This I–V curve was numerically differentiated and normalized in the same way as the experimental data, and the "normalized" spectra for the experimental and computer-modeled data were compared. The shapes and locations of the peaks in the initial input density of states function were chosen so that the calculated $d(\log I)/d(\log V)$ was in reasonable agreement with the experimental curve for Si(111)-(7×7) shown in Figure 4.14c. The other parameters used in the calculation were $\Phi_{\text{sample}} = 2.5$ eV, $\Phi_{\text{tip}} = 2.5$ eV, and $Z = 8.0$ Å.

Figure 4.16 shows the results of this simulation. The DOS function shown in Figure 4.16a was used with Simmon's formulas (assuming a constant DOS for the tip) to generate the I–V curve expected for this distribution, shown in Figure

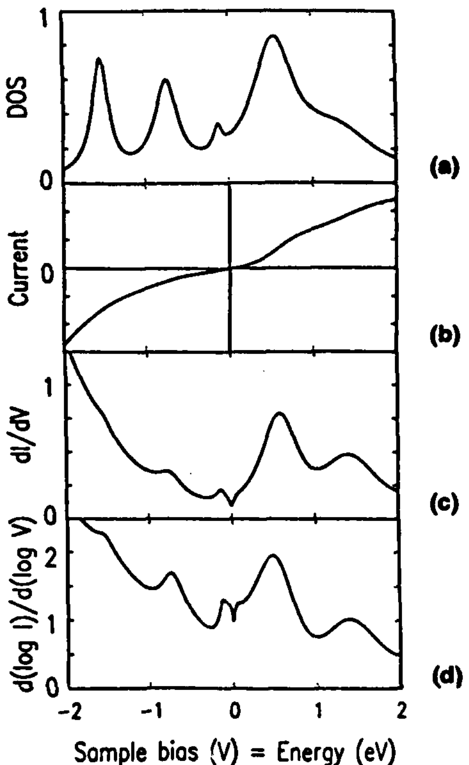

Figure 4.16 Computer modeling of tunneling I–V spectra. **(a)** Input density of states function. **(b)** Tunneling current calculated by numerical integration of Simmon's equation. **(c)** First derivative of tunneling current. **(d)** "Normalized" tunneling spectrum using logarithmic-derivative normalization.

4.16b. This was then numerically differentiated to give the plot of dI/dV vs. V shown in Figure 4.16c, and normalized by the static conductivity to produce the normalized spectrum shown in Figure 4.16d. Comparing this normalized spectrum in the bottom panel with the starting DOS function shown in the top panel shows that they have peaks in nearly the same position. However, the intensities of the peaks are quite different. Unoccupied states of the sample are observed much more clearly and with higher intensity in the normalized tunneling spectra than are occupied states, which is a result of the fact that most of the tunneling electrons arise from states near the Fermi energy of the negatively biased electrode. This numerical simulation demonstrates that the intensities of the peaks observed in in $(dI/dV)/(I/V)$, or equivalently, $d(\log I)/d(\log V)$ are *not* proportional to the surface density of states, particularly at negative sample bias. However, this procedure does provide a *convenient* normalization for the spectroscopy data and is relatively independent of sample–tip separation.

The close correspondence between the simulated spectrum in Figure 4.16d and the normalized experimental data for Si(111)-(7×7) shown in Figure 4.14c indicates that the density of states of Si(111)-(7×7) is similar to the function shown in Figure 4.16a.

When normalizing tunneling spectra of surfaces with a surface-state bandgap, artificial discontinuities arise in this normalization due to the strong voltage dependence of the $B(V)$ term in the denominator of Eq. (4.12), particularly near the band edges. One alternative procedure is then to divide the dynamic conductivity (dI/dV) by the static conductivity (I/V) extrapolated from measurements at higher voltages (outside the surface-state bandgap). This provides compensation for voltage-dependent changes in the tunneling barrier but prevents the denominator in Eq. (4.9) from vanishing.[29] If the structure at the edges of the surface-state bands are of primary importance, direct plots of I vs. V are satisfactory.[20]

Relative Intensities of s, p, and d-Band Contributions

A second significant difference between the density of states detected by STM and the "true" density of states occurs for transition metals. Lang[70] predicted that for transition metals with partially filled d-bands near the Fermi energy, the contribution of these bands to the tunneling current is usually greatly exceeded by the s- and p-band contributions. This has two sources. First, for equivalent principal quantum numbers, d-states tend to be more tightly bound to the nucleus than s- and p-states. Second, for transition metals the occupied d-bands generally have a smaller principal quantum number than the nearby s- and p-bands (4d vs. 5s,5p for Mo, for example). The smaller principal quantum number states decay faster in the vacuum, and so their overlap with the wavefunctions of the tip is often negligible. Lang's calculations indicate that occupied d-states will be nearly invisible to the STM, except for metals near the left edge of the period table (such as Ca), for which the d-states lie at or above the Fermi energy.

The predicted inability of tunneling spectroscopy to observe occupied d-states has been confirmed in several studies. Brodde et al.[71] conducted studies on Au(111), but were not able to observed any structure in the tunneling I–V curves associated with the onset of the d-bands at ≈ 2 eV below E_F. Kuk and Silverman[68] likewise conducted studies of Fe clusters on Au(100) and did not find any observable structure associated with either occupied or unoccupied d-bands previously observed in photoemission and inverse photoemission spectroscopies at 0.6 below and 1.6 eV above E_F.[72] This insensitivity to d-band contributions is unfortunate, as it significantly limits the ability of the STM to distinguish between various transition metals.

Band Structure Effects

In comparing tunneling spectroscopy results with theoretical calculations, it is [illegible] the importance of the band structure of the solid.

The band structure has an effect on tunneling spectroscopy measurements because the rate of decay of the wavefunctions of the sample and tip in the vacuum region is determined by the momentum *perpendicular* to the surface. In Eq. (4.4), the energy E of the state enters the tunneling probability because the effective height of the tunneling barrier depends on the electron energy. More correctly, it depends on the momentum perpendicular to the surface. Using $E = \frac{k^2}{2m} = \left(\frac{k_x^2 + k_y^2 + k_z^2}{2m}\right)$ we can include the effects of nonzero parallel momentum $k_\parallel$ and rewrite the inverse decay length of the wavefunctions as

$$\kappa = \sqrt{2m\bar{\phi}/\hbar^2 + k_\parallel^2} \qquad (4.13)$$

where the average barrier height $\bar{\phi}$ is given by $\bar{\phi} = \sqrt{\left[\frac{(\phi_s + \phi_t)}{2}\right] + \left(\frac{eV}{2}\right) - E}$

and $k_\parallel = \sqrt{k_x^2 + k_y^2}$ is the parallel momentum.

Comparing this expression with the expression given earlier in Eq. (4.4) shows that this essentially amounts to replacing the energy E by $E - \hbar^2\left(\frac{k_\parallel^2}{2m}\right)$. Also, it is apparent from this equation that the wavefunctions have the longest decay length when the parallel momentum is zero, corresponding to the Γ point in the surface Brillouin zone. Thus, tunneling spectroscopy measurements have a built-in preference to probe states at Γ. Detecting tunneling from other locations in the Brillouin zone is most readily done for semiconductors where either the high-lying occupied state disperses upward in energy from Γ, or where the lowest energy unoccupied state disperses downward in energy from Γ. Under these circumstances, energy conservation restricts tunneling at lower voltages to states with nonzero parallel momentum; at higher voltages, tunneling from all states will be possible but will occur preferentially from Γ. For very sharp tips, it is predicted that this preferential tunneling from Γ will be counteracted by momentum broadening through the uncertainty principle due to the strong lateral confinement of the tunneling electrons. This topic will be discussed more in Section 4.62.

Experimental observations of band structure effects have been made for Si(111)-(2×1), which has an unoccupied state dispersing downward from Γ. On this surface, Feenstra et al.[28] found that the effective decay length of the wavefunctions varied strongly as a function of voltage (Fig. 4.15a). A second example comes from ordered overlayers of aluminum on silicon, which also have a downward-dispersion unoccupied state. Figure 4.20 shows both tunneling spectroscopy data as well as theoretical and experimental determinations of the surface band structure. The experimental band structure determination (lower panel, solid dots) shows an unoccupied state that disperses downward in energy from +1.4 eV at Γ to 0.8 eV at K'. The tunneling spectroscopy measurements (upper panel) show a two rather well-defined empty states at +1.0 and +1.4 eV.

The tunneling spectroscopy peak near +1.0 eV corresponds closely to the bottom of the empty band observed near K' in the surface Brillouin zone, while the second peak near +1.4 eV corresponds to the band-edge at $\Gamma(k_\| = 0)$ Here also, the effect is visible mainly because the unoccupied band disperses downward from Γ.

4.5.4 Applications of Local I–V Spectroscopy

In addition to Si(111)-(7×7) work discussed above, the electronic properties of many other clean surfaces and ordered overlayers have been studied using local I–V spectroscopy. Not all of these are review here; rather, we simply highlight some of the more typical measurements to illustrate the capabilities of tunneling spectroscopy.

Tunneling measurements on Si(111)-(2×1)[18, 27, 28, 73] show a close correspondence with the theoretical band structure for the π-bonded chain model proposed by Pandey.[74] Measurements of the inverse decay length as a function of applied bias also have revealed interesting behavior resulting from dispersion of the surface-state bands, which disperse toward E_F as the parallel momentum $k_\|$ increases. At low voltages, tunneling can only occur from states with large $k_\|$, which have a short decay length. At higher voltages, tunneling occurs from states with $k_\| = 0$, which have the slowest decay. From measurements of the inverse decay length as a function of voltage, the dispersion of the surface-state bands could be inferred from the tunneling measurements.

On Si(001)-(2×1),[23, 34] normalized spectra shown in Figure 4.17 reveal a surface-state bandgap of ≈ 0.7 eV, with peaks at −0.85 and +0.35 eV corresponding to the dimer π-bonding and π^*-antibonding states discussed earlier, in agreement with photoemission results.[65, 66] Tunneling measurements show that exposure of this surface to NH_3 eliminates these states and replaces them with an intense state lying 1.1 eV above E_F associated with Si–H antibonding states[34] due to dissociation of the NH_3. Voltage-dependent imaging also provides a contrast between reacted and unreacted dimers, due to changes in the spatial distribution of occupied states on H adsorption.

Kubby et al.[25] reported tunneling spectroscopy measurements on the Ge(001) surface as well. Figure 4.18 shows their measurements on Ge(001) obtained at two different stabilization voltages. The normalized spectra overlap and lead to the identification of three surface states, at −2.6, −0.9, and +1.05eV.

Figure 4.19 shows the capability of atomic-resolution I–V measurements to directly probe the electronic properties of defects. This figure shows I–V curves acquired at different distances from a small defect, measured simultaneously with the constant-current topograph (at −1.5 eV).[75] Far away from the defect (9e,9f), the tunneling I–V curve shows a clear gap as revealed from the sharp turn-on of the tunneling current near −0.45 and +0.25 eV (in agreement with the gap edges observed in area-averaged, logarithmically differentiated spec-

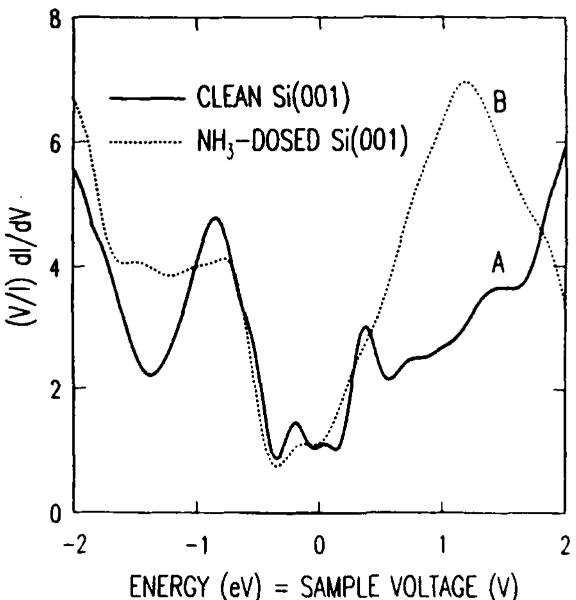

Figure 4.17 Normalized tunneling spectra on clean Si(001) and Si(001) after dosing with NH_3. The clean surface has an occupied state near −0.35 eV and an empty state near +0.5 eV; after dosing, these states are eliminated and replaced with a single, Si-H state at +1.5 eV. (Reprinted with permission from Ref. [34].)

tra[34]). As the defect is approached, the sharp gap edges disappear and directly over the defect (9c), the tunneling curve exhibits a strong exponential increase both above and below E_F, demonstrating that there is a high density of states at E_F at the defect site.[75] Such spatially dependent measurements also provide a direct measure of the spatial extent of the wavefunctions associated with defects and impurities.

Single-atom defects occurring in Al overlayers on Si(111) have also been studied.[43, 67, 76] Figure 4.20a shows tunneling I-V measurements made on Al adatoms and Figure 4.20b shows the I–V measurements on the Si adatoms, compared with a theoretical calculation[44] of the band structure for Al adatoms on Si(111). Substituting Si for Al shifts the energy of a p_Z state from +1.1 to −0.35 eV, which is readily detectable in the I–V spectra and also leads to large contrast changes in constant-current topographs that were noted earlier and shown in Figure 4.8. Unique localization effects are also observed in tunneling spectra at these defects, which are effectively isolated from one another by the large surface atom spacing in the $\sqrt{3}$ structure.[43, 76]

The ability to probe the local electronic structure of defects and chemically inequivalent atoms at surfaces has great potential for the study of surface chemical reactivity on an atom-by-atom basis. An example is the decomposition

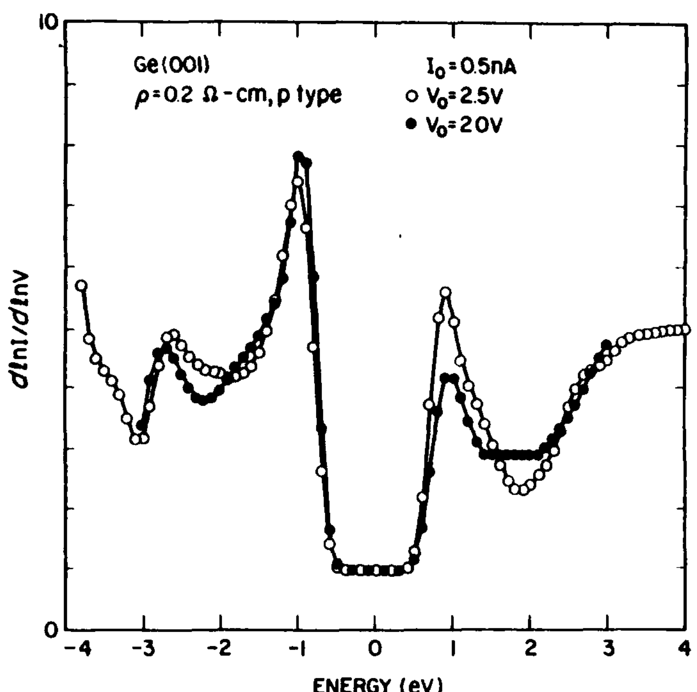

Figure 4.18 Tunneling spectra on p-type Ge(001) acquired using different stabilization voltages and subsequently normalized. Due to the absence of tunneling within the surface-state bandgap, the spectra were forced to unity at the lowest voltages. (Reprinted with permission from Ref. [25].)

of NH_3 on Si(111)-(7×7) studied by Avouris and Wolkow.[77, 78] The Si(111)-(7×7) structure has several types of chemically inequivalent surface atoms exposed. By combining voltage-dependent STM topographs with local *I–V* measurements before and after exposing the surface to NH_3, variations in chemical reactivity between the various types of chemically inequivalent atoms were identified. Thus, local *I–V* spectroscopy provides a way of directly correlating chemical reactivity with local electronic structure.

With the advent of high-temperature superconductivity, many investigators have applied tunneling spectroscopy to studies of both normal high-temperature superconductors. Several studies have reported spatial variations in superconducting energy gaps. Fein et al.[79] and Kirtley et al.[61] measured *I–V* curves at each location while scanning over granular superconductors, and later analyzed the data to provide an image of the spatial dependence of the energy gap.

Perhaps one of the most dramatic applications of STM has been the recent work of Hess et al.,[62, 80] who used local tunneling spectroscopy to image the

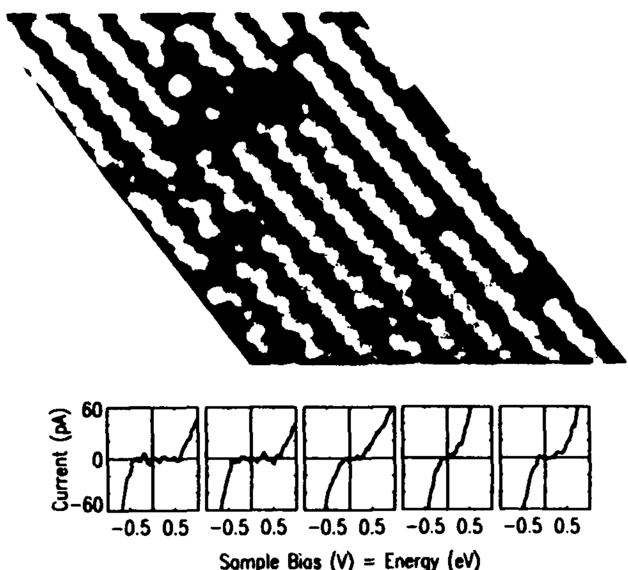

Figure 4.19 Spatial dependence of tunneling *I–V* curves on Si(001). Far away from defect, *I–V* curve shows a clear bandgap. Above the defect, the *I–V* curve is "metallic" in nature. The spatial extent of this metallic character is ≈ 7 Å. (Reprinted with permission from Ref. [14].)

electronic state density around a superconducting flux core in $NbSe_2$. Many other recent studies of superconductors have concentrated on the various new high-temperature superconductors[81–84] as well as organic superconductors.[85]

4.6 General Features of Tunneling Spectra

4.6.1 Dynamic Range

To a first approximation, tunneling *I–V* curves are exponential in voltage for $V \gtrsim 100$ m V. As a result of this exponential dependence, one difficulty commonly encountered in tunneling spectroscopy measurements is that of dynamic range. Assuming a constant density of states for sample and tip, the tunneling current is roughly given by

$$I \propto \int_0^V \exp(-AZ\sqrt{\Phi - V}) \quad (4.14)$$

where $A = 1.025\ eV^{-1/2}\ Å^{-1}$. Figure 4.21 shows the result of numerically integrating this equation for several different values of average work function Φ. In each case, the sample–tip distance has been adjusted such that the

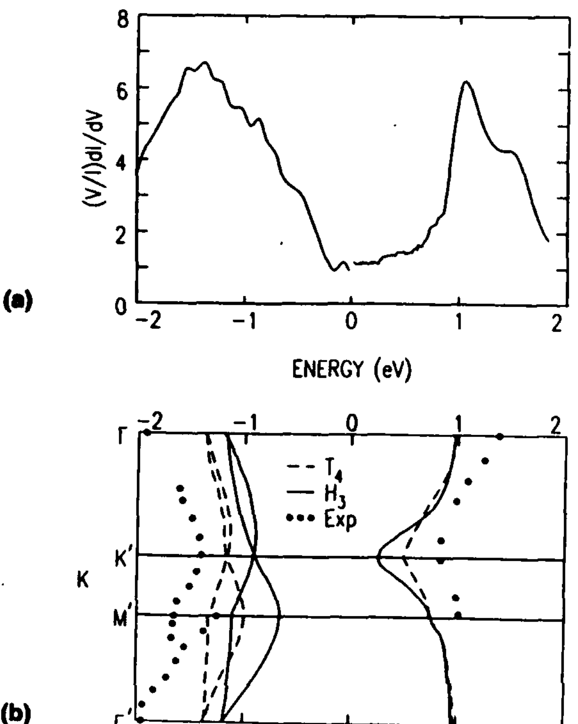

Figure 4.20 (a) Tunneling spectra on $(\sqrt{3}\times\sqrt{3})$-Al/Si(111). (b) Calculated and experimental surface-state bandstructures for $(\sqrt{3}\times\sqrt{3})$-Al. (Reprinted with permission from Ref. [76].) The double peak for the unoccupied state observed in STM likely arises from a band-structure effect.

tunneling current is 0.85 nA at $V = 2.0$ V. Here, we see that the sample with the *highest* work function has an I–V curve that is somewhat more linear than the sample with the lowest work function. Qualitatively, this is easy to understand. For a material with a high work function, increasing the applied voltage leads to only a relatively small change in the argument of the exponent, and the integral tends to be comparatively linear. For a material with a *low* work function, however, increasing the applied voltage makes the exponential factor significantly greater, and the integral increases as a very rapid exponential function. In each case, however, even in the limit of constant density of states one must have at least three orders of magnitude dynamic range in the tunneling current measurement in order to record the electronic characteristics between about 0.1 and 2 eV.

One way around this difficulty has been successfully utilized by Feenstra and Stroscio[63] to measure the density of states within the surface-state bandgap on

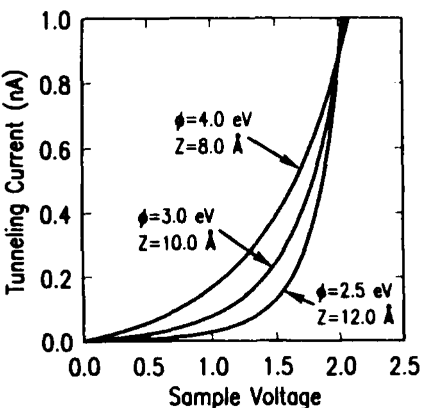

Figure 4.21 Calculated tunneling I–V curves for different values of barrier height and sample–tip separation. The spectra were all calculated such that I_{tunnel}=0.85 nA at a sample voltage of 2 V.

GaAs(110). Since here the density of states near the Fermi level is very low, the dynamic range problem is much worse than the situation described above, where the density of states was assumed to be continuous. To permit measurements over a very wide dynamic range, Feenstra and Stroscio abandoned the idea of performing measurements at constant sample–tip separation; instead, they allowed the separation to change, but by measuring both the current and the sample–tip separation as a function of voltage, and by measuring the tunneling barrier height, it is possible to effectively normalize the data to a constant sample-tip separation through the tunneling equations.

4.6.2 Resolution

The resolution of tunneling spectroscopy is determined primarily by the range of electron energies that can contribute to the tunneling current. For inelastic tunneling experiments at low voltages, Hansma[7] determined an effective resolution of $5.4kT$, or approximately 140 m V at room temperature. For electronic spectroscopy at higher voltages, the effective resolution is primarily determined by the fact that the electrons involved in tunneling arise from a broad range of energies, determined by the voltage difference between sample and tip. The width of the electron energy distribution can be seen from Eq. (4.4) for the transmission probability $T(E,eV)$. Since the work functions of sample and tip are large, the argument of the exponent is relatively insensitive to E, resulting in a wide energy distribution for the tunneling electrons. Thermal effects can be included by multiplying the tunneling transmission factor by the Fermi function $f(E)$, which describes the probability that a state with energy E is occupied. The definition of $f(E)$ is

$$f(E) = \frac{1}{1 + \exp\left[\frac{E - E_F}{kT}\right]} \tag{4.15}$$

Since electrons must tunnel from an occupied state to an unoccupied state, the overall tunneling transmission probability must be multiplied by two Fermi functions:

$$T(E,eV,T) = T(E,eV)f(E)[1 - f(eV - E)] \tag{4.16}$$

The first factor is the temperature-independent transmission probability $T(E,eV)$ defined in Eq. (4.4), the second factor is the probability that the state with energy E on the first electrode (either sample or tip) is occupied, and the third factor is the probability that the state with energy $eV - E$ on the second electrode (either tip or sample) is unoccupied; energy conservation is implied, since the Fermi level of sample and tip are different by an amount eV.

Figure 4.22 shows the relative transmission probability as a function of energy assuming that $\phi_s = \phi_t = 4.0$ eV, $Z = 8.0$ Å, and the applied bias $V = 2.0$ V. The dotted line is the calculation neglecting thermal broadening, while the solid line is calculated including thermal broadening for $T = 300$ K. It can be seen that the main effects of including finite temperature are to broaden out the Fermi edge and to shift the electron energy distribution to slightly lower energies. In either case, it can be seen that most of the tunneling electrons comes from within 300 mV of the Fermi level of the negatively biased electrode. The asymmetric

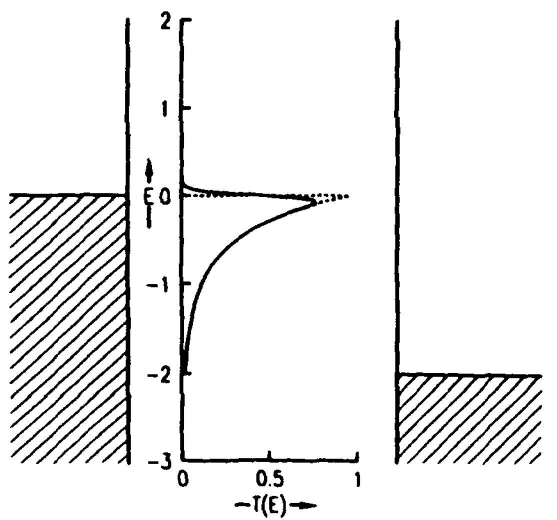

Figure 4.22 Energy distribution of tunneling electrons, calculated using Eq. (4.4) and assuming $\phi_s = \phi_t = 4.0$ eV, $Z = 8.0$ Å, and $V = 2.0$ V. Dotted curve neglects thermal broadening, while the solid line includes thermal broadening for $T = 300$ K.

form of $T(E,eV)$, with the sharp increase at E_F, helps to make the effective resolution of the STM somewhat higher when probing empty states of the sample than when probing filled states.

An additional broadening mechanism may arise from the Heisenberg uncertainty principle, for extremely sharp tips. The localization of the tunneling current to a region Δw of approximately 5 Å diameter implies an uncertainty of $\approx 1/\Delta w = 0.2$ A−1 in the parallel momentum $k_\parallel$ of the tunneling electrons. Since the two-dimensional Brillouin zone for the Si(111)-(7×7) surface, for example, has a maximum length of 0.155 Å−1 (along the ΓK' direction), this can represent a significant averaging over various portions of the surface Brillouin zone. For highly dispersive states, this will tend to contribute an additional energy-broadening mechanism since tunneling will no longer be strongly preferred from the Γ point.

4.6.3 Tip Electronic Structure

Many of the current limitations in tunneling spectroscopy arise from the inability to easily prepare well-defined tips of known electronic structure. While uncharacterized tips remain the rule, progress continues to be made in the area by combining field ion microscopy and field evaporation techniques with STM.[86, 87] Kuk and Silverman[86] utilized well-controlled tips to study the influence of tip size on the measured STM topographic resolution. For tunneling spectroscopy, it is essential not only to prepare a tip with a known geometric configuration, but also to determine the electronic structure of this tip. The unusual bonding geometry and small size of the STM tip are expected to significantly modify its electronic structure from that of a bulk material. A number of groups[88-91] have recently been active calculating the electronic structure of the tip and its effects on the tunneling current and tunneling spectra. Ultimately, it may be possible to perform tunneling spectroscopy experiments with tips of known geometric and electronic structure. The tunneling spectra are always a convolution of the electronic structures of the sample and tip. For these reasons, it is usually necessary to compare tunneling spectra acquired at different locations on the surface in order to distinguish the spatially invariant contribution of the tip and the spatially varying contribution from the sample.

4.6.4 Anomalies

Just as in conventional scanning tunneling microscopy, there are a number of anomalies and artifacts that can arise in tunneling spectroscopy experiments. Many of these anomalies arise because of the general lack of control over the geometry and electronic structure of the tip. One of the most interesting analysis of tip effects in tunneling spectroscopy has been performed by Klitsner et al.[92] On a tip that (on the basis of topographic images) was composed of at least two "microtips," they acquired tunneling spectroscopy data as a function of sample-

tip separation and at different locations on the sample. At particular locations, tunneling from one "microtip" was strongly favored over the other. Through a detailed analysis of these tunneling spectra acquired at different locations on a nominally homogeneous sample, it was possible to distinguish the contributions from each microtip.

In general, tip-related artifacts cannot be easily ruled out in any tunneling spectroscopy measurement. When making comparisons between spectra at two different locations on the surface (with the same tip), the electronic structure of the tip is known to be at least constant. In making absolute measurements, however, it is very important to perform measurements using a variety of different tips and samples to validate the results.

Negative Differential Resistance

Simple one-dimensional tunneling theory between electronically equivalent electrodes generally predicts that tunneling transmission probability increases monotonically with the applied voltage. Since in most cases structure in the density-of-states is relatively weak, the net result is that the tunneling current generally increases with the applied voltage. However, this is not mandated by the tunneling equations. It is quite possible (over certain limited ranges of applied voltage) for the tunneling current to *decrease* as the applied voltage is increased. This phenomenon is referred to as "negative differential resistance" (or "NDR") because the differential resistance dI/dV is negative in these regions.

Negative differential resistance is of particular interest due to the fact that the "Esaki tunnel diode" utilizes this same effect to make microwave oscillators and other high-frequency semiconductor devices.

The observation of negative differential resistance over localized areas with the scanning tunneling microscope was first reported by Hamers and Koch,[93] who reported NDR in localized regions of ≈ 5–10 Å diameter on partially-oxidized silicon surfaces, as shown in Figure 4.23. Here, the tunneling curve increases normally at low voltages, but at approximately 1 V sample bias, the tunneling current exhibits a clear *decrease;* the corresponding first derivative (Fig. 4.23b) becomes negative.

Negative differential resistance can have several origins. First, it can occur if the tunneling transmission function is not a monotonically increasing function of $|V|$. This is the case for partially oxidized silicon surface, which form localized "trap" states throughout the band gap region. These trap states give rise to the anomalous I–V curves and negative differential resistance observed in Figure 4.23. In this case, NDR is observed at positive sample bias, when electrons tunnel from the tip to the sample. The origin of this behavior is illustrated in Figure 4.24. Here, the trap energy lies well above the Fermi energy of the sample. At low bias voltages the trap is unoccupied and the the tunneling I–V curve is comparatively [illegible]. At sufficiently positive sample bias, however, electrons from the [illegible] the trap and occupy this trap state. One unique

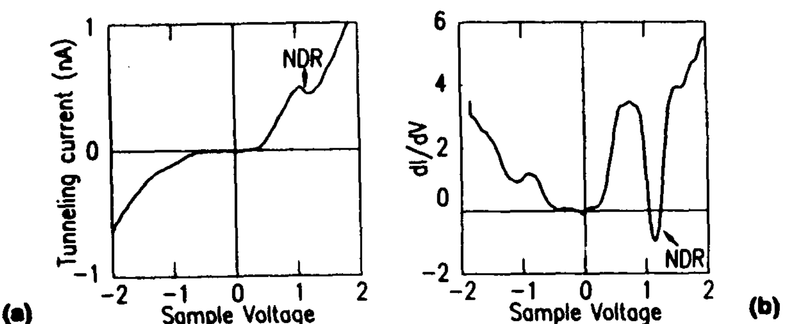

Figure 4.23 **(a)** Tunneling I–V curve demonstrating negative differential resistance (NDR), acquired at an oxide "trap" approximately 5 Å diameter on oxidized Si(001). **(b)** First derivative of the tunneling I–V curve. (Reprinted with permission from Ref. [93].)

characteristic of these trap states is that they can capture an electron for a very long time (easily in the millisecond regime).[94] The negative charge associated with the electron captured in this localized trap state acts as a "Coulomb blockade," preventing further electrons from tunneling until the electron relaxes from the trap state to the Fermi energy. As long as the lifetime of the electron in the trap state is longer than ≈10−10 (the average time between tunneling events for a current of 1 nA), then it can easily give rise to very strong negative differential resistance. As a result, the tunneling transmission function increases at low voltages (Fig. 4.24a), decreases sharply when the trap is near the Fermi energy, and becomes occupied by tunneling electrons (Fig. 4.24b) and then increases again at higher bias voltages.

A second cause of NDR can be the existence of energetically narrow states on either the sample or tip. If the density of states of sample or tip has sufficiently sharp structure, then over a particular range of bias voltages the *decrease* in the

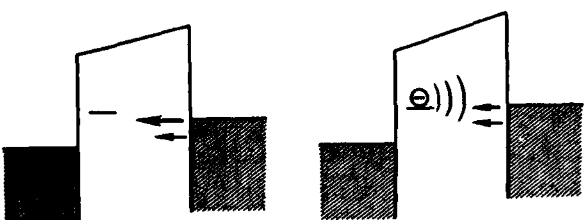

Figure 4.24 Origin of negative differential resistance due to trap states on partially oxidized silicon surfaces. At low voltage, tunneling electrons do not have sufficient energy to occupy the trap state, and tunneling is normal. At slightly higher voltage, the trap becomes occupied, and exerts a "Coulomb repulsion," which prevents further tunneling and gives rise to NDR.

density of states near the Fermi energy can overwhelm the *increase* in the voltage-dependent tunneling transmission probability, resulting in a net decrease in tunneling current. Bedrossian et al.[95] and Lyo et al.[96] reported NDR on highly B-doped Si samples and attributed it to the presence of energetically localized states. This NDR can also occur from localized states on the *tip*, since sample and tip play nearly equivalent roles in STM.

Tip-Induced Band-Bending

In typical STM measurements, there is a very high electric field between the sample and tip. On semiconductor surfaces, Weimer et al.[97] suggested that the electric field between tip and sample can change the band-bending, as illustrated in Figure 4.25 The significance of this effect depends to a great extent on the density of states within $\simeq kT$ of the Fermi energy, since any tendency to change the band-bending will chance the occupation of these states. On Si(111)-(7×7), the presence of an adatom-related surface state at the Fermi energy keeps the Fermi level well pinned at a constant position. Thus, the tunneling spectra[2] show surface state energies in good agreement with the values obtained using other surface science techniques. On most other semiconductors, however, the surface reconstruction results in a surface-state bandgap. As a result, the Fermi-level position at most semiconductor surfaces is determined by defects or the tails of the bulk bands. On Si(001), for example, one particular kind of common defect *has a high density of states and pins the Fermi level. With* comparatively low numbers of midgap states available to pin the Fermi level, it is quite possible for the tip-induced electric field to affect the band energies. If this occurs, then the full sample–tip potential drop does not occur across the vacuum, but occurs partially in the bulk. As a result, the tunneling spectra will spread out, with all peaks appearing further away from the Fermi energy than anticipated. On some surfaces the tunneling spectra have been shown to be in good agreement with the results of other surface science techniques,[2, 28] indicating that tip-induced

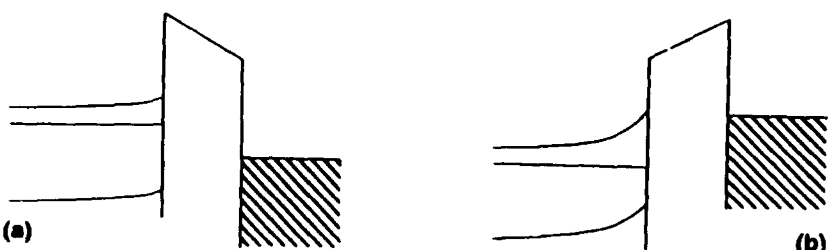

Figure 4.25 Tip-induced band-bending at unpinned, n-type semiconductor surfaces. At negative sample bias (**a**), the Schottky barrier is reduced (forward-biased) and the tunneling current is high. At positive sample bias (**b**), the Schottky barrier is increased and the tunneling current is reduced. On p-type samples the situation is reversed.

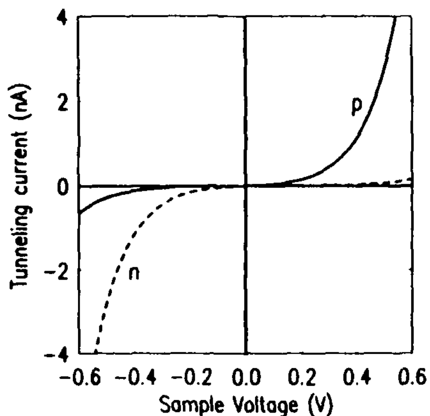

Figure 4.26 Effect of tip-induced band-bending on tunneling current. On n-type samples, tunneling current is high at negative sample bias and low at positive bias. On p-type samples, the situation is reversed. (After Ref. [98].)

band-bending is negligible. On wider bandgap material and unpinned surfaces, it can be significant.

Kaiser et al.[98] showed that on hydrogen-terminated silicon surfaces, the very low density of gap states leaves the Fermi level unpinned. Under those conditions, the electric field between tip and sample penetrates a significant distance into the bulk of the sample, and thereby modifies the energies of the valence and conduction bands. As illustrated in Figure 4.25, on an n-type sample a midgap Fermi level implies upward bending of the bands at the surface; as a result, at positive sample bias the band-bending will be increased, and at negative bias the band-bending will be decreased. On a p-type sample the situation is reversed. As shown in Figure 4.26, Kaiser et al. found that the band-bending produced pronounced differences between the general shape of the *I–V* curves on n-type and p-type material. One result of tip-induced band-bending is that even in the absence of discrete surface-state related electronic structure, the tunneling *I–V* curves will be asymmetric at positive and negative bias and will also be different on n-type and p-type material. As demonstrated by Kaiser et al., this band-bending can be modeled as a Schottky barrier problem.

4.7 Other Spectroscopies

4.7.1 Inelastic Tunneling Spectroscopy

The electronic spectroscopy discussed thus far provides some chemical contrast, but is not capable in most cases of actually identifying chemical species adsorbed on a surface. For such purposes, it would be more useful to measure the

vibrational spectra of adsorbed species, since vibrational spectra are usually very sharp and show features that are characteristic of particular molecular functional groups. Theoretical calculations[14,99–101] have predicted that under certain circumstances, changes in dI/dV as large as 10% might be observed in tunneling measurements. Observing such structure is not an easy task because the vibrational features are so sharp that a low-temperature STM is required in order to avoid thermal broadening of the Fermi levels. Hansma[7] estimated an effective resolution of $5.4kT$ for inelastic tunneling, while vibrational features are typically only a few meV wide; as result, measurement of vibrational losses must be performed at liquid helium temperature or lower.

Early experimental studies reported inelastic losses associated with phonons on graphite[102] and sorbic acid vibrations adsorbed on graphite,[103] both obtained on a surface that was completely immersed in liquid helium. In the case of graphite phonons, a good correspondence was observed between peaks in d^2I/dV^2 vs V and the known phonon energies determined from various other methods. For sorbic acid adsorbed on graphite, peaks were observed in the *first* derivative spectrum instead of the expected second derivative spectrum. Additionally, the peaks were very intense and the energies of the peaks were different from those measured in bulk tunnel junctions. The origins of these discrepancies are not yet resolved and may arise from a strong coupling with graphite bulk states.

More recently, Gregory[104] clearly observed vibrational-inelastic features in a "self-assembled tunnel junction." Although not strictly a "scanning" tunneling microscope, this junction is formed by two fine crossed wires with a layer of adsorbed argon between, forming a tunnel junction of atomic dimensions. Small amounts of hydrocarbon contamination are present in the argon, which can be detected through inelastic losses characteristic of carbon–hydrogen molecular vibrations. Figure 4.27 shows the second derivative of the tunneling current, $\frac{d^2I}{dV^2}$ obtained by Gregory. Clear inelastic features are observed at 359 mV (2900 cm−1) and in a range near 173 mv (1400 cm^{-1}). The former, higher energy peak corresponds closely with the energy expected for C-H stretching modes, while the second corresponds to a broad range of energies typically associated with C-H bending modes. The spectral widths of the observed features were typically on the order of 20 mV (≃ 160 cm^{-1}), due to a combination of both homogeneous and inhomogeneous line broadening mechanisms. Additionally, Gregory showed that the first derivative dI/dV of the tunneling current varies linearly with the applied voltage (and the current itself is quadratic in V). This same functional dependence was predicted by Averin and Likharev[105] for a Coulomb blockade. Such a blockade results when the lateral scale of the tunnel junction is so small that the flow of electrons across the gap is correlated, due to their Coulomb repulsion. This observation provides strong evidence for the "atomic" scale of the self-assembled tunnel junction. The failure to observe similar vibrational spectra in conventional low-temperature scanning tunneling microscopes remains a question of great interest and importance.

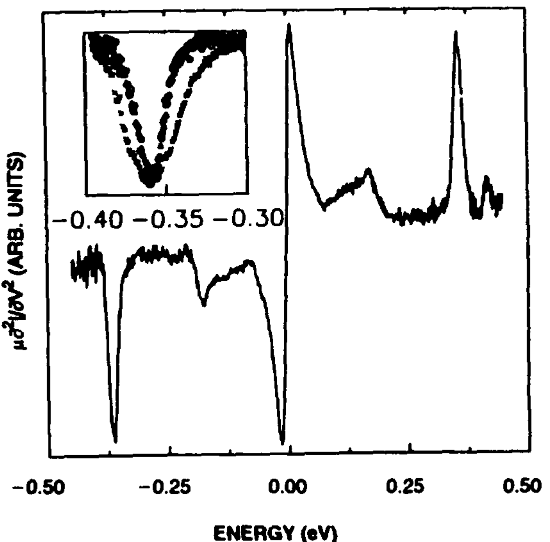

Figure 4.27 Inelastic tunneling spectra obtained on "self-assembled" tunnel junction. Characteristic vibrational losses are observed near 359 and 173 mV associated with hydrocarbon vibrations. (Reprinted with permission from Ref. [104].)

4.7.2 Barrier Height Spectroscopy

In conventional tunneling spectroscopy the tunneling current is measured as a function of the applied voltage, providing a measure of the sample density of states. One of the major uncertainties in such experiments is that the effective height and width of the the tunneling barrier are generally unknown. However, it is possible to directly probe the effective tunneling barrier height. Although this technique has received comparatively little attention, it provides information complementary to tunneling I–V spectroscopy. Barrier height spectroscopy involves measuring the dependence of the tunneling current on the sample–tip separation, at constant applied voltage. In its usual implementation, a constant bias is applied between the sample and tip. A small modulation (typically a few hundredths of an angstrom) is applied to the Z-piezo, and the resulting modulation in the tunneling current is measured using a lock-in amplifier. The frequency of the modulation must be faster than the closed-loop bandwidth of the STM feedback electronics, but must be small compared to the mechanical resonance frequency of the piezoelectric scanners. Typically the modulation frequency is chosen to be just slightly faster than the feedback electronics.

As in the case of tunneling I–V spectroscopy, the tunneling current can be written as

$$I = \int_0^{eV} \rho_s(r,E)\rho_t(r,E - eV)T(E,eV,r)dE \qquad (4.17)$$

where $T(E,eV,r)$ is the probability that when a voltage V is applied between sample and tip, an electron with energy E will tunnel across the barrier. In the WKB tunneling formula for planar electrodes, the tunneling transmission probability $T(E,eV)$ for electrons with energy E and applied bias voltage V is given by[18, 106]

$$T(E,eV,r) = \exp\left(-\frac{2Z\sqrt{2m}}{\hbar}\sqrt{\frac{\phi_s + \phi_t}{2} + \frac{eV}{2} - E}\right), \tag{4.18}$$

where ϕ_s and ϕ_t are the *local* work functions of sample and tip, respectively, and Z is the sample–tip separation, m is the electron mass, and $\hbar = \frac{h}{2\pi}$ where h is Planck's constant. At low bias voltages, eV is approximately zero and $E = E_F$, so that this simplifies as

$$T = \exp\left(-\frac{2Z\sqrt{2m}}{\hbar}\sqrt{\frac{\phi_s + \phi_t}{2}}\right). \tag{4.19}$$

Thus, the tunneling transmission probability can be directly related to the *local* work function ϕ_s of the sample. Rewriting the equations shows that

$$\frac{dI/dZ}{I} = \frac{2\sqrt{2m}}{\hbar}\sqrt{\phi_s + \phi_t}. \tag{4.20}$$

Thus, by modulating the z-piezo and measuring the induced modulation (dI/dZ) of the tunneling current I, the average work function of sample and tip can be determined. Since the work function of the tip is constant, lateral variations in the measured barrier height can be attributed to changes in the local sample work function. In practice, many experimental determinations of barrier heights using this technique have obtained unreasonably small values. At the time of this writing, it appears that several effects may be entering, depending on the experimental conditions.

The first reason for anomalously low barrier heights is the detailed form of the potential function between the tip and the sample. As a result of the close proximity of tip and sample, there is an image potential that has been predicted to modify the potential. However, as Binnig,[107] Coombs,[108] and Lang [109] have pointed out, even though the form of the potential function includes image potential terms that vary as $1/Z$, in determining the tunneling barrier height these terms cancel, leaving only terms that vary like $1/Z^2$. At the distances encountered in STM, the image potential is expected to have negligible effect on the measured barrier heights; this has been further confirmed by Coombs et al.,[108] who numerically integrated Simmon's tunneling equations[69] and concluded that the effect of the image potential was negligible under normal STM conditions.

More recently, Lang[109] pointed out that the potential function may be regarded as the sum of an electrostatic potential $v_{ES}(r)$ and an exchange-correlation potential $v_{XC}(r)$. In the local density approximation, the potential varies as the cube root of the electron density. Thus, while the electron density in the vacuum region varies like $n = n_0 e^{-AZ\sqrt{\Phi}}$, the exchange-correlation potential

contribution to the total potential varies like $v_{XC} \propto e^{-AZ/3\sqrt{\Phi}}$. Lang performed numerical calculations of the tunneling current as a function of distance using this local density approximation, and used the results to generate an effective barrier height. As shown in Figure 4.28, the results indicate that for sample–tip separations of less than 12 Bohr (about 6.5 Å), the measured "barrier height" will be substantially below the true work function.

Another reason for anomalous barrier heights is the mechanical interaction between sample and tip. This is illustrated with the help of Figure 4.29, which shows data of Hamers on the measured barrier height as a function of sample–tip separation using a tungsten tip and a clean, Si(111)-(7×7) surface under ultrahigh vacuum conditions.[110] At large distances, the measured barrier height of ≈3.6 eV is in good agreement with the value anticipated from the work functions of tungsten and silicon. As the sample–tip separation is decreased, the barrier height is constant at first; it then shows a small *increase*, and shortly thereafter plunges toward zero. At extremely small distances, the sample and tip are in obvious physical contact. Clearly, when the sample and tip are in physical contact, then as the Z-piezo scanner tries to push the tip toward the sample the only effect is to slightly compress the sample–tip physical junction, with little effect on the resistance of the junction; thus, the barrier height must tend toward zero when the sample and tip are in physical contact.

As the tip is moved toward the sample from larger distances, Figure 4.29 shows that the measured barrier height actually *increases* slightly. One explana-

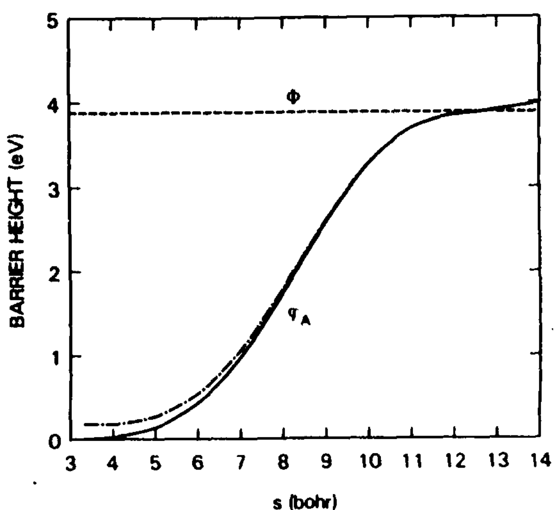

Figure 4.28 Calculation by Lang of the effective barrier height as a function of sample tip separation. The comparatively slow approach to the equilibrium work function value is due primarily to the exchange-correlation part of the atomic potential. (Reprinted with permission from Ref. [109].)

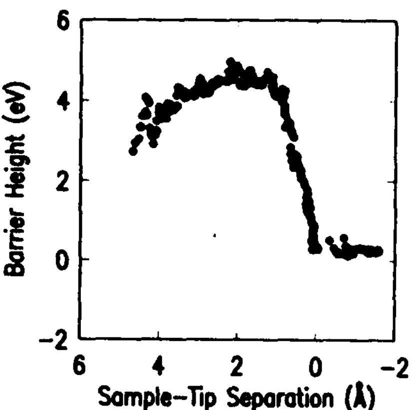

Figure 4.29 Experimental measurement of the barrier height as a function of sample–tip separation on a clean Si(111)-(7×7) surface with a tungsten tip. At close distances (corresponding to strong mechanical contact) the barrier drops to nearly zero. (Reprinted with permission from Ref. [110].)

tion for this effect has been proposed by Chen[110] as indicative of an attractive force between the sample and tip leading to *mechanical* deformation. The initial assumption is that the sample–tip interaction can be modeled as a Morse-type potential. When the sample–tip separation corresponds to the steep, attractive part of the potential, then as the Z-piezo pushes the tip toward the surface (during each period of the applied Z-piezo modulation), the atom at the end of the tip experiences a greater attraction toward then surface than it does when it is 180° out-of-phase, in effect "stretching" the tip slightly. The net result of this is that the separation between the sample and the atom at the end of the tip actually changes by slightly *more* than the Z-piezo modulation, leading to an barrier height which is slightly *larger* than the true work function when the sample–tip interaction is attractive. The prediction of this analysis is that the measured barrier height will be too large when the sample–tip separation corresponds to being on the attractive part of the Morse potential, it will be exactly equal to the true value when the sample–tip separation corresponds to the minimum of the Morse potential, and it will be smaller than the true work function at smaller distances when the potential becomes repulsive (in effect, compressing the tip and/or sample). Chen successfully fit the detailed shape of this function, assuming only that the mechanical interaction can be described with a Morse potential with two free parameters.

Atomic-scale geometric contributions to the measured barrier height arise from a "smoothing" of the equipotential contours in the vacuum. As discussed earlier in this chapter (Fig. 4.9) the effective decay length of the wavefunctions above a surface protrusion must be shorter than that above a depression, since the potential corrugations always decrease at large distances from the sample.

Since a shorter decay length is essentially equivalent to a high effective barrier, this means that (all other factors being equal) the barrier height measured above a protrusion will be larger than that measured above a depression.

Finally, it must be remembered that the equation used for the barrier height assumes that the separation between sample and tip is modulated by δZ. On tilted samples or samples where the surface normal is tilted by θ with respect to the Z-direction (as defined by the direction of expansion of the Z-piezo), the modulation of the gap spacing is $\delta Z_{gap} = \cos(\theta)\delta Z_{piezo}$. For surfaces that are not atomically smooth, this convolutes a strong geometric factor into the barrier height measurement proportional to the cosine of the local sample tilt.

4.8 Summary

In this chapter, several of the methods that have been developed for acquiring and interpreting tunneling spectroscopy data have been presented and discussed, together with some representative examples of how each of these techniques can be applied to study the electronic structure of surfaces. The unique ability of the STM to directly probe the electronic structure of surfaces promises to open yet another dimension in our understanding of surfaces by allowing us to study the energetics of the electronic states at the surface on an atom-by-atom basis and to directly correlate the geometric positions of the atoms with the resulting electronic structure. Proper analysis of tunneling spectroscopy data is crucial to the effective use of this powerful technique. Advances in the acquisition and interpretation of tunneling spectroscopy data continue to improve our ability to make efficient use of this capability.

Acknowledgments

I would like to express my appreciation to Norton Lang, Jerry Tersoff, Randy Feenstra, Julian Chen, Joe Demuth, and David Cahill, all of whom have had a continuing interest in tunneling spectroscopy. Additionally, I would like to express appreciation to the U.S. Office of Naval Research for partial support of this work.

References

1. G. Binnig, H. Rohrer, C. Gerber, and E. Weibel, *Phys. Rev. Lett.* **50**, 120 (1983).
2. R. Hamers, R. Tromp, and J. Demuth, *Phys. Rev. Lett.* **56**, 1972 (1986).
3. R. Tromp, R. Hamers, and J. Demuth, *Phys. Rev. B* **34**, 1388 (1986).
4. R. M. Feenstra, W. A. Thompson, and A. P. Fein, *Phys. Rev. Lett.* **56**, 608 (1986).
5. R. Feenstra, J. Stroscio, J. Tersoff, and A. Fein, *Phys. Rev. Lett.* **58**, 1192 (1987).

6. N. Lang, *IBM J. Res. Dev.* **30**, 374 (1986).
7. P. Hansma, *Tunneling Spectroscopy: Capabilities, Applications, and New Techniques.* Plenum Press, New York, 1982.
8. E. Wolf, *Electron Tunneling Spectroscopy.* Oxford University Press, Oxford, 1986.
9. C. Duke and W. Ford, *Surf. Sci.* **111**, L685 (1981).
10. N. Garcia, F. Flores, and F. Guinea, *J. Vac. Sci. Technol.* **6**, 323 (1988).
11. J. Tersoff and D. Hamann, *Phys. Rev. B* **31**, 805 (1985).
12. J. Tersoff and D. Hamann, *Phys. Rev. Lett.* **50**, 1998 (1983).
13. A. Baratoff, *Physica* **127B**, 143 (1984).
14. B. Persson and A. Baratoff, *Phys. Rev. Lett.* **59**, 339 (1987).
15. N. Lang, *Phys. Rev. B* **34**, 5947 (1986).
16. C. J. Chen, *J. Vac. Sci. Technol.* **6**, 319 (1988).
17. G. Binnig, K. Frank, H. Fuchs, N. Garcia, B. Reihl, H. Rohrer, F. Salvan, and A. Williams, *Phys. Rev. Lett.* **55**, 991 (1985).
18. J. Stroscio, R. Feenstra, and A. Fein, *J. Vac. Sci. Technol. A* **5**, 838 (1987).
19. A. Selloni, P. Carnevali, P. Tosatti, and C. Chen, *Phys. Rev. B* **31**, 2602 (1985).
20. R. Hamers and U. Koehler, *J. Vac. Sci. Technol. A* **7**, 2854 (1989).
21. R. Tromp, E. Van Loenen, J. Demuth, and N. Lang, *Phys. Rev. B* **37**, 9042 (1988).
22. R. Hamers, R. Tromp, and J. Demuth, *Surface Sci.* **181**, 346 (1987).
23. R. Hamers, P. Avouris, and F. Bozso, *J. Vac. Sci. Technol.* **6**, 508 (1988).
24. R. Hamers, R. Tromp, and J. Demuth, *Phys. Rev. B* **34**, 5343 (1987).
25. J. Kubby, J. Griffith, R. Becker, and J. Vickers, *Phys. Rev. B* **36**, 6079 (1987).
26. R. Becker, J. A. Golovchenko, and B. Swartzentruber, *Phys. Rev. Lett.* **55**, 987 (1985).
27. J. Stroscio, R. Feenstra, and A. Fein, *Phys. Rev. Lett.* **57**, 2579 (1986).
28. R. Feenstra, J. Stroscio, and A. Fein, *Surf. Sci.* **181**, 295 (1987).
29. R. Feenstra and P. Martensson, *Phys. Rev. Lett.* **61**, 447 (1988).
30. J. Stroscio, R. Feenstra, and A. Fein, *Phys. Rev. Lett.* **58**, 1668 (1987).
31. D. Biegelsen, R. Bringans, J. Northrup, and L. Swartz, *Phys. Rev. B* **41**, 5701 (1990).
32. D. K. Biegelsen, L. I. Swartz, and R. D. Bringans, *J. Vac. Sci. Technol. A* **8**, 280 (1990).
33. B. Reihl, J. Gimzewski, J. Nicholls, and E. Tosatti, *Phys. Rev. B* **33**, 5770 (1986).
34. R. Hamers, P. Avouris, and F. Bozso, *Phys. Rev. Lett.* **59**, 2071 (1987).
35. J. Appelbaum, G. Baraff, and D. Hamann, *Phys. Rev. Lett.* **35**, 11 (1975).
36. J. Chadi, *Phys. Rev. Lett.* **43**, 43 (1979).
37. K. Pandey, *Phys. Rev. Lett.* **47**, 1913 (1981).
38. K. Takayanagi, Y. Tanishiro, M. Takahashi, and S. Takahashi, *J. Vac. Sci. Technol. A* **3**, 1502 (1985).
39. [illegible] and A. Fein, *J. Vac. Sci. Technol. A* **6**, 497 (1988).

40. M. D. Pashley, K. W. Haberern, W. Friday, J. M. Woodall, and P. D. Kirchner, *Phys. Rev. Lett* **60**, 2176 (1988).
41. K. W. Haberern and M. D. Pashley, *Phys. Rev. B* **41**, 3226 (1990).
42. J. Stroscio, R. Feenstra, and A. Fein, *Phys. Rev. B* **36**, 7718 (1987).
43. R. Hamers, *J. Vac. Sci. Technol. B* **6**, 1462 (1988).
44. J. Northrup, *Phys. Rev. Lett.* **53**, 683 (1984).
45. R. Becker, T. Klitsner, and J. Vickers, *J. Microsc.* **152**, 157 (1988).
46. R. Becker and J. Vickers, *J. Vac. Sci. Technol. A* **8**, 226 (1990).
47. H. Bando et al., *J. Vac. Sci. Technol. A* **6**, 344 (1988).
48. E. van Loenen, J. Demuth, R. Tromp, and R. Hamers, *Phys. Rev. Lett.* **58**, 373 (1987).
49. R. Hamers, *Phys. Rev. B* **40**, 1657 (1989).
50. J. Demuth, U. Koehler, R. Hamers, and P. P. Kaplan, *Phys. Rev. Lett.* **62**, 641 (1989).
51. G. Binnig and H. Rohrer, *Surf. Sci.* **157**, L373 (1985).
52. N. Garcia, *IBM J. Res. Dev.* **30**, 533 (1986).
53. E. Louis, F. Flores, and P. Echenique, *Phys. Scripta* **37**, 359 (1988).
54. W. Kaiser and R. Jaklevic, *IBM J. Res. Dev.* **30**, 411 (1985).
55. R. Garcia, J. Saenz, and N. Garcia, *Phys. Rev. B* **33**, 4439 (1986).
56. F. Salvan, H. Fuchs, A. Baratoff, and G. Binnig, *Surf. Sci.* **162**, 634 (1985).
57. R. Becker, B. Swartzentruber, and J. Vickers, *J. Vac. Sci. Technol.* **6**, 472 (1988).
58. R. Becker, T. Klitsner, and J. Vickers, *Phys. Rev. B* **38**, 3537 (1988).
59. A. Humbert, F. Salvan, and C. Mouttet, *Surf. Sci.* **181**, 307 (1987).
60. G. Van de Walle, H. Van Kempen, P. Wyder, and C. Flipse, *Surf. Sci.* **181**, 27 (1987).
61. J. Kirtley, S. Raider, R. Feenstra, and A. Fein, *Appl. Phys. Lett.* **50**, 1607 (1987).
62. H. Hess, R. Robinson, R. Dynes, J. Valles, and J. Waszczak, *Phys. Rev. Lett.* **62**, 214 (1989).
63. R. Feenstra and J. Stroscio, *J. Vac. Sci. Technol. B* **5**, 923 (1987).
64. T. Berghaus, A. Brodde, H. Neddermeyer, and S. Tosch, *Surf. Sci.* **193**, 235 (1988).
65. F. Himpsel and T. Fauster, *J. Vac. Sci. Technol. A* **2**, 815 (1984).
66. T. Fauster and F. Himpsel, *J. Vac. Sci. Technol. A* **1**, 1111 (1983).
67. R. Hamers and J. Demuth, *J. Vac. Sci. Technol. A* **6**, 512 (1988).
68. Y. Kuk and P. Silverman, *J. Vac. Sci. Technol. A* **8**, 289 (1990).
69. J. Simmons, *J. Appl. Phys.* **34**, 1793 (1963).
70. N. Lang, *Phys. Rev. Lett.* **58**, 45 (1987).
71. A. Brodde, S. Tosch, and H. Neddermeyer, *J. Microsc.* **152**, 441 (1988).
72. J. Callaway and C. Wang, *Phys. Rev. B* **16**, 2095 (1977).
73. R. Feenstra, W Thompson, and A. Fein, *Phys. Rev. Lett.* **56**, 608 (1986).
74. K. Pandey, *Proceedings of the 17th International Conference on the the Physics of Semiconductors.* Springer-Verlag, New York, 1985.

75. R. Hamers, *J. Vac. Sci. Technol.* (1987). R. J. Hamers, *J. Vac. Sci. Technol.*, in press.
76. R. Hamers and J. Demuth, *Phys. Rev. Lett.* **60**, 2527 (1988).
77. P. Avouris and R. Wolkow, *Phys. Rev. B* ??, ?? (????).
78. R. Wolkow and P. Avouris, *Phys. Rev. Lett.* **60**, 1049 (1988).
79. A. Fein, J. Kirtley, and R. Feenstra, *Rev. Sci. Inst.* **58**, 10 (1987).
80. H. Hess, R. Robinson, R. Dynes, J. V. Mr, and J. Waszczak, *J. Vac. Sci. Technol. A* **8**, 450 (1990).
81. M. Tanaka, S. Yamazaki, M. Fujinami, T. Takahashi, H. Katayama-Yoshida, W. Mizutani, K. Kajimura, and M. Ono, *J. Vac. Sci. Technol. A* **8**, 475 (1990).
82. M. Gallagher and J. Adler, *J. Vac. Sci. Technol. A* **8**, 464 (1990).
83. T. Oshio, J. Tanaka, A. Ono, T. Nagamura, Y. Kamizono, Y. Sakai, and S. Ehara, *J. Vac. Sci. Technol. A* **8**, 468 (1990).
84. T. Endo, H. Yamada, T. Sumomogi, K. Kuwahara, T. Fujita, and S. Morita, *J. Vac. Sci. Technol. A* **8**, 468 (1990).
85. H. Bando, S. Kashiwaya, H. Tokumoto, H. Anzai, N. Konoshita, and K. Kajimura, *J. Vac. Sci. Technol. A* **8**, 479 (1990).
86. Y. Kuk and P. Silverman, *Appl. Phys. Lett.* **48**, 1597 (1986).
87. T. Sakurai, T. Hashizume, Y. Hasegawa, I. Kamiya, N. Sano, K. Yokoyama, H. Tanaka, I. Sumita, and S. Hyodo, *J. Vac. Sci. Technol. A* **8**, 324 (1990).
88. K. Kobayashi and M. Tsukada, *J. Vac. Sci. Technol. A* **8**, 170 (1990).
89. S. Ciraci, A. Baratoff, and I. P. Batra, *Phys. Rev. B* **41**, 2763-75 (1990).
90. D. Lawunmi and M. C. Payne, *J. Phys.* **2**, 3811 (1990).
91. J. Tersoff, *Phys. Rev. B* **41**, 1235 (1990).
92. T. Klitsner, R. Becker, and J. Vickers, *Phys. Rev. B* **41**, 3837 (1990).
93. R. Hamers and R. Koch, *Physics and Chemistry of SiO and the Si-SiO Interface.* Plenum Press, New York, 1989.
94. R. Koch and R. Hamers, *Surf. Sci.* **181**, 333 (1987).
95. P. Bedrossian, D. Chen, K. Mortensen, and J. Golovchenko, *Nature (London)* **342**, 258 (1989).
96. I. W. Lyo and P. Avouris, *Science* **245**, 1369 (1989).
97. M. Weimer, J. Kramar, and J. Baldeschwieler, *Phys. Rev. B* **39**, 5572 (1989).
98. W. Kaiser, L. Bell, M. Hecht, and F. Grunthaner, *J. Vac. Sci. Technol. A* **6**, 519 (1988.).
99. G. Binnig, N. Garcia, and H. Rohrer, *Phys. Rev. B* **32**, 1336 (1985).
100. B. Persson and J. Demuth, *Solid State Commun.* **57**, 769 (1986).
101. A. Baratoff and B. Persson, *J. Vac. Sci. Technol.* **6**, 331 (1988).
102. D. Smith, G. Binnig, and C. Quate, *Appl. Phys. Lett.* **49**, 1641 (1986).
103. D. Smith, M. Kirk, and C. Quate, *J. Chem. Phys.* **86**, 6034 (1987).
104. S. Gregory, *Phys. Rev. Lett.* **64**, 689 (1990).
105. D. Averin and K. Likharev, *J. Low Temp. Phys.* **62**, 345 (1985).
106. R. Hamers, *Annu. Rev. Phys. Chem.* **40**, 531 (1989).

107. G. Binnig and H. Rohrer, *Rev. Mod. Phys.* **59**, 615 (1987).
108. J. Coombs, M. Welland, and J. Pethica, *Surf. Sci.* **198**, L353 (1988).
109. N. Lang, *Phys. Rev. B* **37**, 10395 (1988).
110. R. J. Hamers, *J. Vac. Sci. Technol.*, submitted for publication.